Atmospheric CO_2 estimates for the last 17 million years based on foraminiferal $\delta^{11}B$ at Ocean Drilling Program Sites 806 and 807 in the Western Equatorial Pacific

Maxence Guillermic[1,2], Sambuddha Misra[3,4], Robert Eagle[1,2], Aradhna Tripati [1,2]

[1]Department of Atmospheric and Oceanic Sciences, Department of Earth, Planetary, and Space Sciences, Center for Diverse Leadership in Science, Institute of the Environment and Sustainability, University of California – Los Angeles, Los Angeles, CA 90095 USA

[2]Laboratoire Géosciences Océan UMR6538, UBO, Institut Universitaire Européen de la Mer, Rue Dumont d'Urville, 29280, Plouzané, France

[3]The Godwin Laboratory for Palaeoclimate Research, Department of Earth Sciences, University of Cambridge, UK

[4]Indian Institute of Science, Centre for Earth Sciences, Bengaluru, Karnataka 560012, India

Correspondence to: Maxence Guillermic (maxence.guillermic@gmail.com) and Aradhna Tripati (atripati@g.ucla.edu)

ABSTRACT

Constraints on the evolution of atmospheric CO_2 levels throughout Earth's history are foundational to our understanding of past variations in climate. Despite considerable effort, estimates of past CO_2 levels do not always converge. Here we reconstruct atmospheric CO_2 values across major climate transitions over the past 17 million years using the boron isotopic composition ($\delta^{11}B$) of planktic foraminifera from 89 samples obtained from two sites in the West Pacific Warm Pool, Ocean Drilling Program (ODP) Sites 806 and 807. These sites are in a region that today is in equilibrium with the atmosphere, despite equatorial divergence, and is likely to have been in equilibrium with the atmosphere for the interval studied. We use high-precision multi-collector inductively-coupled plasma mass spectrometry and show that data from these sites can reproduce the ice core record. Estimates of early Miocene pCO_2 are generally higher than published reconstructions from other sites, while values for the Pliocene and Pleistocene are more similar to other datasets. We find evidence for reductions in pCO_2 of ~280 µatm during the Middle Miocene Climate Transition, ~270 µatm during Pliocene Glacial Intensification, and ~50 µatm during the Mid-Pleistocene Climate Transition. There is possible evidence for a larger reduction in glacial pCO_2 during the Mid-Pleistocene Transition compared to interglacial pCO_2, and a minimum in pCO_2 during glacial MIS 30. Our results are consistent with a strong coupling between pCO_2, temperature and ice sheet expansion throughout the past 17 million years.

Highlights

In this study, we are able to accurately reproduce pCO_2 data from ice cores, demonstrating the fidelity of our approach. We therefore apply the same framework to older samples to create a long-term pH and pCO_2 reconstruction for the past 17 million years. We find major increases in surface water pH and decreases in atmospheric pCO_2 were associated with decreased temperature in the Western Equatorial Pacific, including associated with major episodes of ice sheet expansion in the high latitudes, providing more robust quantitative constraints on the past coupling between pCO_2, temperature, and cryosphere stability.

Keywords

Boron isotopes, CO_2, ODP Site 806, ODP Site 807, Miocene, climate

1. Introduction

Due to concerns about the long-term consequences of anthropogenic emissions and associated climate change (IPCC, 2014, 2018), efforts have been made to quantify past atmospheric CO_2 and examine past relationships between CO_2 and temperature. Such data are not only critical for constraining Earth-system sensitivity (Lea, 2004; Lunt et al., 2010; Pagani et al., 2010; Hansen et al., 2012, 2013, Foster and Rohling, 2013; Schmittner et al., 2011; Tierney et al., 2020), but are also of broad interest because such data can help us understand the evolution of climate and geological systems through Earth's history (Tripati et al., 2011; Foster et al., 2017; Tripati and Darby, 2018). However, discrepancies between proxy reconstructions still exist, including for major climate transitions of the Cenozoic. In particular, there remains a pressing need for robust and higher-resolution atmospheric CO_2 records from sites that are in equilibrium with the atmosphere.

Relatively high-resolution and direct determinations of atmospheric CO_2 are available for the last 800 kyr through analysis of air bubbles extracted from ice-cores, but these records are limited to the availability of cores (Petit et al., 1999; Siegenthaler et al., 2005; Luthi et al., 2008). A window into atmospheric CO_2 levels comes from 1 million-year-old blue ice (Higgins et al., 2015) and more recently from the Pliocene period (Yan et al., 2019). Most reconstructions of CO_2 for prior to 800 ka are based on indirect terrestrial and marine proxies. Stomata indices for fossil leaves (Van der Burgh, 1993; Royer , 2001), carbon isotope ratios ($\delta^{13}C$) of paleosols (Retallak et al., 2009), $\delta^{13}C$ of alkenones (Pagani et al., 2005; Zhang et al., 2013), B/Ca ratios of surface-dwelling foraminifera (Yu and Hönisch, 2007; Foster, 2008; Tripati et al., 2009, 2011), and boron isotope ratios ($\delta^{11}B$) of surface-dwelling foraminifera (Pearson and Palmer., 2000; Hönisch et al., 2009; Bartoli et al., 2011; Foster et al., 2012; Foster and Sexton, 2014; Chalk et al., 2017; Sosdian et al., 2018) have been used to estimate atmospheric CO_2.

Each of the above proxy methods has sources of systematic errors that we do not attempt to exhaustively document as they have been discussed in-depth elsewhere (e.g., Pagani et al., 2005; Tripati et al., 2011; Guillermic et al., 2020). However, we note that significant developments in the boron-based proxies include improvements to the accuracy and precision of measurements using multi-collector inductively coupled mass spectrometry (MC-ICP-MS) compared to early work with thermal ionization mass spectrometry (TIMS), where there were large instrumental mass fractionations and challenges with laboratory intercomparison (Foster et al., 2013; Farmer et al., 2016; Aggarwal and You, 2017). There

was also the realization that temperature-dependent K_D to interpreting B/Ca sensitivities observed from the field of sediment trap, core-top, and downcore studies (Yu and Hönisch, 2007; Foster et al., 2008; Tripati et al., 2009, 2011; Babila et al., 2010; Osborne et al., 2020) differ from foraminiferal culture experiments (Allen et al., 2011, 2012) and inorganic calcite (Mavromatis et al., 2015); this type of discrepancy has also been observed with other elemental proxies (e.g., Mg/Ca). Such differences may be due to differences in growth rates (Sadekov et al., 2014), ontogenetic changes, a correlation in the field between temperature and other hydrographic variables that obscure robust statistical determination of parameter relationships, culture conditions resulting in organisms being stressed, and/or other factors.

The marine CO_2 proxy that appears to be subject to the fewest systematic uncertainties is the boron isotopic composition ($\delta^{11}B$) of planktic foraminifera as measured using MC-ICPMS and TE-NTIMS. This proxy provides constraints on seawater pH, if temperature, salinity, seawater $\delta^{11}B$, and the appropriate mono-specific calibration between $\delta^{11}B_{carbonate}$ and $\delta^{11}B_{borate}$ are constrained (Pearson and Palmer., 2000; Foster et al., 2008; Sosdian et al., 2018; Raitzsch et al., 2018; Guillermic et al., 2020). Seawater pH can be used to calculate seawater pCO_2 if there are constraints on a second parameter of the carbonate system (e.g. alkalinity, DIC). Atmospheric pCO_2 can then be constrained if the site being examined is in air-sea CO_2 equilibrium.

Given the evolution of the field, the number of studies generating high-precision and high-resolution boron-based records over major climate transitions in the Cenozoic using the recent analytical methods, and incorporating our current understanding of proxy systematics are relatively few (Foster et al., 2012; Martinez-Boti et al., 2015b; Chalk et al., 2017, de la Vega et al., 2020). Furthermore, of the existing studies using boron-based proxies, an additional uncertainty frequently exists, namely the short time interval of study (e.g., emphasizing on a climate transition) (Martinez-Boti et al., 2015b; Chalk et al., 2017) and whether the study sites remain in air-sea CO_2 equilibrium with the atmosphere (Martinez et al., 2015a). And although estimation of atmospheric pCO_2 from seawater pH using this proxy is relatively straightforward, reconstructions are still impacted by uncertainties including the lack of robust constraints on a second parameter of the carbonate system, and our limited understanding of secular variations in the $\delta^{11}B$ of seawater (Tripati et al., 2011; Sosdian et al., 2018; Greenop et al., 2017).

Therefore, to provide additional constraints on the evolution of atmospheric pCO_2 from the Miocene through recent, we developed new records from the western tropical

Pacific. We use foraminiferal $\delta^{11}B$ and trace elements in the planktic foraminiferal species *Trilobus sacculifer* and *Globigerinoides ruber* to reconstruct past seawater pH and atmospheric CO_2 at Ocean Drilling Program (ODP) Sites 806 and 807 in the Western Equatorial Pacific (WEP) over the last 17 million years (myr). The two sites we examined are located on the western border of the tropical Pacific Ocean, the largest open-oceanic region on the globe, and the warmest open ocean region at present. Currently this region is in air-sea CO_2 equilibrium despite equatorial divergence (Takahashi et al., 2014).

This work represents the first reconstructions of past seawater pH and pCO_2 for the WEP using MC-ICPMS, thereby providing an invaluable new perspective on reconstructing past atmospheric CO_2 via marine sediment archives. We explore various constraints on the second carbonate system parameter using a number of different scenarios, following on the systematic work done by Tripati et al. (2009) and (2011) for B/Ca. We interpret these data using recent constraints on seawater $\delta^{11}B$ (Lemarchand et al., 2000; Raitzsch and Hönisch, 2013; Greenop et al., 2017). For temperature estimation, we utilize a multi-variable model for Mg/Ca (Gray and Evans, 2019), that builds on prior work with clumped isotopes in planktic foraminifera for Site 806 and other WEP sites demonstrating that for the Last Glacial Maximum to recent, salinity-corrected Mg/Ca values are needed to yield convergent estimates of mixed-layer temperatures (Tripati et al., 2014).

2. Materials and Methods

Below we describe site locations, analytical methods used, and figures of merit. The supplemental methods section describes screening for potential contamination, equations used for calculations, and error propagation.

2.1 Site locations

Samples are from three ODP holes recovered during ODP Leg 130 in the WEP (Fig. 1, Table 1): ODP 806A (0°19.140'N, 159°21.660'E, 2520.7 m water depth), ODP 806B (0°19.110'N, 159°21.660'E, 2519.9 m water depth), and ODP 807A (3°36.420'N, 156°37.500'E, 2803.8 m water depth) (Berger et al., 1993). Sites 806 and 807 are not likely to have experienced major tectonic changes over the last 20 million years.

The WEP sites used in this study are currently close to equilibrium with the atmosphere (Takahashi et al., 2014) (despite equatorial divergence), and given their location, are likely to have remained so throughout the study interval. We do note, however, that the

thermocline is deep today, and that changes in thermocline depth have been inferred for the WEP (Nathan and Leckie., 2009; Ford et al., 2015). Any potential changes in depth and properties coupled with changes in upwelling, have the potential to influence equilibrium at this site. While this is the case, changes could be smaller in the WEP compared to other regions, due to the relatively small amplitude changes in temperature and salinity (e.g., compared to higher latitude sites, or eastern boundary current regions).

2.2 Age models

Sites 806 and 807 have high quality age models (Shackleton et al., 1991). The age model for Site 806 from 0-1.35 Ma is based on Lea et al. (2000), while from 1.352-5.875 Ma it is based on Lisiecki and Raymo, (2005), and Wara et al. (2005) is the source of information for sediments older than 5.875 Ma. Ages for Site 807 are based on published biostratigraphy (Berger et al., 1993) for 807 with additional constraints placed by Zhang et al., (2007) for the interval from 0-0.550 Ma.

2.3 Species and trace element cleaning

Samples were picked and cleaned to remove clays at UCLA (Los Angeles, CA) and the University of Western Brittany (Plouzane, France). 50-100 foraminifera shells were picked from the 300-400µm fraction size for *T. sacculifer* (w/o sacc) and from the 250-300 µm for *G. ruber* (white sensu stricto). Picked foraminifera were gently crushed, clays removed, and checked for coarse-grained silicates. Samples were then cleaned using a full reductive and oxidative cleaning protocol following Barker et al. (2003). A final leach step with 0.001N HCl was done prior dissolution in 1N HCl. Boron purification used a published microdistillation protocol (see Misra et al., 2014b, Guillermic et al., 2020 for more detailed methods).

2.4 Chemical purification and geochemical analysis

Chemical separation was performed in a boron-free clean lab at the University of Cambridge (Cambridge, UK). Calcium concentrations were measured on an ICP-AES ®Ultima 2 HORIBA at the Pôle Spectrometrie Océan (PSO), UMR6538 (Plouzané, France). Elemental ratios (e.g. X/Ca ratios) were analyzed on a Thermo Scientific ®Element XR HR-ICP-MS at the PSO, Ifremer (Plouzané, France). Boron isotopic measurements were carried

out on a Thermo Scientific ®Neptune+ MC-ICP-MS equipped with 10^{13} amplifiers (Lloyd et al., 2018) at the University of Cambridge (Cambridge, UK).

2.5 Standards

Variations in B isotope ratios are expressed in conventional delta (δ) notation with $\delta^{11}B$ values reported against the reference standard NIST SRM 951 (NIST, Gaithersburg, MD, USA):

$$\delta^{11}B\ (‰) = 1000 \times \left(\frac{^{11}B/^{10}B_{Sample}}{^{11}B/^{10}B_{NIST\ SRM\ 951}} - 1\right) \qquad \textbf{eq. 1}$$

Multiple analyses of external standards were performed to ensure data quality. For boron isotopic measurements, JCP-1 (Geological Survey of Japan, Tsukuba, Japan, Gutjahr et al., 2014) was used as a carbonate standard, and NEP, a *Porites sp* coral from University of Western Australia and Australian National University was also used (McCulloch et al., 2014). A boron isotope liquid standard, ERM© AE121 (certified $\delta^{11}B$ = 19.9 ± 0.6 ‰, SD), was used to monitor reproducibility and drift during each session (Vogl and Rosner, 2012; Foster et al., 2013; Misra et al., 2014b). For trace elements, external reproducibility was determined using the consistency standard Cam-Wuellerstorfi (University of Cambridge) (Misra et al., 2014b).

2.6 Figures of Merit

2.6.1 $\delta^{11}B$ analyses

Samples measured for boron isotopes typically ranged in concentration from 10 ppb B (~5ng B) to 20 ppb B samples (~10ng B). Sensitivity was 10mV/ppb B (eg. 100mV for 10ppb B) in wet plasma at 50µl/min sample aspiration rate. The intensity of ^{11}B for a sample at 10ppb B was typically 104 ± 15 mV (2 SD, typical session) closely matched the 98 ± 6 mV (2 SD, typical session) of the standard. Procedural boron blanks ranged from 15 pg B to 65 pg B (contributed to less than <1% of the sample signal). The acid blank during analyses was measured at ≤ 1mV on the ^{11}B (which also is < 1% of the sample intensity), and no memory effect was seen within and across sessions.

External reproducibility was determined by analyzing the international standard JCP-1 (Gutjahr et al., 2014) and a *Porites sp.* coral (NEP). The boron isotopic composition of JCP-1 was measured at 24.06 ± 0.20‰ (2 SD, n=6) within error of published values of 24.37 ± 0.32‰, 24.11± 0.43‰ and 24.42 ± 0.28‰ from Holcomb et al. (2015), Farmer et al. (2016)

and Sutton et al. (2018), respectively. Average values are $\delta^{11}B_{NEP}$ = 25.72 ± 0.79‰ (2 SD, n=31) determined over 13 different analytical sessions, with each number representing a separately processed sample from this study. These results are within error of published values of 26.20 ± 0.88‰ (2 SD, n = 27) and 25.80 ± 0.89‰ (2 SD, n = 6), from Holcomb et al. (2015) and Sutton et al. (2018), respectively. Data are reported in Table 2.

2.6.2 X/Ca analyses

Trace element (TE) analyses were conducted at a Ca concentration of either 10 or 30 ppm. Typical blanks for a 30 ppm Ca session were: ^{7}Li < 2%, ^{11}B < 7%, ^{25}Mg < 0.2% and ^{43}Ca < 0.02%. Additionally, blanks for a 10 ppm Ca session were: ^{7}Li < 2.5%, ^{11}B < 10%, ^{25}Mg < 0.4% and ^{43}Ca < 0.05%. Analytical uncertainty of a single measurement was calculated from the reproducibility of the CamWuellestorfi standard: 0.6 µmol/mol for Li/Ca, 8 µmol/mol for B/Ca and 0.02 mmol/mol for Mg/Ca (2 SD, n=48). Data are reported in Table 2.

2.7 Calculations

Details of calculations are in the Supplemental methods. We explored multiple scenarios for the evolution of seawater $\delta^{11}B$ and alkalinity for calculations of pCO_2. During the interval overlapping with the ice core record, we observe that the choice of model used does not make a significant difference in reconstructed values (Fig. S2). During earlier time intervals, we see there is a greater divergence, reflecting larger uncertainties in seawater $\delta^{11}B$ and alkalinity further back in Earth history.

During the early Pliocene (~4.5 to 3.5 Ma) and prior to 10 Ma, calculations of pCO_2 diverge largely because of disagreement between studies estimating past seawater $\delta^{11}B$ (Fig. S2). However, we also found that reconstructed pH values that utilize each of the $\delta^{11}B_{seawater}$ histories are not significantly different, when the uncertainty in reconstructed pH is fully propagated (Fig. S2 and S3; see also Hönisch et al., 2019). In contrast to the results from Greenop et al. (2017), the record from Raitzsch and Hönisch, (2013) exhibits substantial variations on short timescales. Such variability is a challenge to reconcile with the Li isotope record of Misra and Froelich, (2012), given that Li has a shorter residence time than boron while having similar sources and sinks. For the remainder of this study, we use the $\delta^{11}B_{seawater}$ history from Greenop et al. (2017) because it is in good agreement with seawater δ^{7}Li (Misra and Froelich, 2012).

The three alkalinity models used diverge prior to 9 Ma, with a maximum difference at ~13 Ma that is also reflect in reconstructed pCO_2 (Fig. S3). However, all three models yield pCO_2 estimates that are within error of each other when the full uncertainty is considered (Fig. S3). For the remainder of the text, we utilize the model of Caves et al. (2016) for alkalinity and the $\delta^{11}B_{seawater}$ determined by Greenop et al. (2017), as these represent the best constrained histories for each available at this time.

3. Results and discussion

3.1 Reproducing pCO_2 from ice cores

Validation of air-sea equilibrium in the WEP during the relatively large amplitude late Pleistocene glacial/interglacial cycles was a primary goal for our work. In order to validate our approach, we reconstructed pCO_2 for the last 800 kyr (Fig. 2). The two critical diagnostics we use for method validation are: 1) that the reconstruction of pCO_2 is representative of recent atmospheric CO_2, and 2) that the boron-based reconstruction empirically reproduces the record from ice cores. As shown in Fig. 2, absolute values for the last glacial/interglacial cycle are within error of the ice core record (Petit et al., 1999 and others) at both sites. For the last 800 kyr, reconstructed pCO_2 values for Holes 806A and B and Site 807 are within error of the Vostok ice core (Petit et al., 1999 and others). Between MIS 7 and 6, our reconstructions exhibit a decrease in temperature (ΔT) of 2.4°C, an increase in pH (ΔpH) of 0.08 and a decrease in pCO_2 ($\Delta pCO2$) of 58 µatm. Between stage 3 and 1, we observed an increase of temperature of 2.5°C, a decrease of pH of 0.13 and an increase in pCO_2 of 76 µatm. These results highlight that we are able to reproduce absolute measurements of atmospheric pCO_2 within error of the ice core record, and reproduce the amplitude of changes between transitions, with uncertainties typical for this type of work (Hönisch et al., 2019). We note that reconstructed pCO_2 uncertainties could potentially be reduced using independent temperature proxies for the WEP such as clumped isotope thermometry (Tripati et al., 2010; 2014), a technique that is not sensitive to the same sources of error as Mg/Ca thermometry, and therefore is an area planned for future work.

3.2 Long–term record for the past 17 myr

Our reconstruction is consistent with published Mg/Ca estimates of early Pliocene to recent temperatures at Site 806 (Medina-Elizalde et al., 2005, Wara et al., 2005; Tripati et al., 2009, 2011). Our reconstruction is also consistent with the work of Nathan and Leckie,

(2009) for time slices at ~7.3 and ~6.2 Ma, though we note that the SST in our study is slightly higher (~2°C) than what was reported for the middle/late Miocene by Nathan and Leckie, 2009 and Zhang et al., 2014, which could reflect the different methods used for reconstructing temperature. Our temperature record over the last 17 myr for the WEP (Fig. 3C) shows a gradual decrease between 17 and 6.5 Ma from 36.7°C ± 0.6°C (2 SD, n=4) for the Miocene Climate Optimum (MCO) to values of 28.8 ± 3.4°C (2 SD, n=67) over the last 6.5 myr. From 6.5 Ma to present, we reconstruct a slight decrease in SSTs, with more variability after the Mid-Pleistocene Transition (MPT). Raw $\delta^{11}B$ data (Fig. S1B) exhibit a significant decrease (4.2‰) with increasing age for *T. sacculifer* from 16.5 Ma to present. Reconstructed pH for the MCO are 7.80 ± 0.10 (SD, n=4), with an increase of ~0.27 to a Holocene value of 8.18 ± 0.11 (n=2) (Fig. 3D).

3.3 Miocene

The study of Miocene (23-5.3 Ma) climate is thought to provide a useful analog for changes associated with global warming and melting of polar ice, in concert with ocean circulation (Holbourn et al., 2013). The Miocene epoch is characterized by a warm interval, the Miocene Climate Optimum (~17-14 Ma - MCO), and an abrupt cooling during the Middle Miocene Climate Transition (~15-13 Ma – MMCT) that led to the expansion of ice on Antarctica and Greenland. Climate modeling supports a role for decreasing CO_2 in this transition (DeConto and Pollard, 2003). However, proxies for CO_2 yield conflicting reconstructions for the MCO and MMCT. Alkenone-based reconstructions do not show any variations over the MCO and MMCT with pCO_2 below 300 ppm (Zhang et al., 2013). However, it is a challenge to simulate the large-scale advance and retreat of Antarctic ice with such low pCO_2 values (Gasson et al., 2016). In contrast, published $\delta^{11}B$-based reconstructions supports higher pCO_2 for the MCO of ~350-400 ppm (Foster et al., 2012), 300-500 ppm (Greenop et al., 2014) or ~470-630 ppm (Sosdian et al., 2018), although it is unclear if these values accurately reflect the atmosphere given the sites may or may not have been in equilibrium with the atmosphere.

Some of the highest pCO_2 values we reconstruct are during the MCO (Fig. 3E). For the MCO, our estimates are 479 ± 173 µatm (2 SD, n=4, Table 3). The middle Miocene values we reconstruct are in line with previous studies (Greenop et al., 2014; Sosdian et al., 2018). Sosdian et al. (2018) report values of 470 to 630 ppm depending on the model of $\delta^{11}B_{seawater}$ chosen. We attribute the differences in $\delta^{11}B$-based pCO_2 to the choice of

reconstruction methods and/or the different oceanographic settings at each site. All of the boron isotope-based reconstructions do not support reconstructions from alkenones for the Miocene (Pagani et al., 1999; 2005; Zhang et al., 2013). As thoughtfully discussed by Badger et al. (2019), the response of CO_2 derived from alkenones is muted compared to boron-based reconstructions of CO_2, and this is possibly due to changes in coccolithophore calcification based on recent studies (Bolton and Stoll, 2013; Bolton et al., 2016). During the MCO relative maxima in pCO_2, our data support very warm sea surface temperatures in the WEP (36.7°C ± 0.6°C 2SD, n=4; Fig. 5C), that merits further examination in future studies. In fact, the highest temperatures recorded in our samples occur when there is a minimum in the global composite record of $\delta^{18}O$ of benthic foraminifera (Zachos et al., 2001, 2008; Tripati and Darby, 2018).

During the MMCT, we find evidence for changes in pCO_2 and temperature in the WEP (Fig. 4). Fom 13.5 to 12.9 Ma, we reconstruct an increase of pH ~0.24 and a major decrease of pCO_2 of ~243 µatm during an interval highlighted by Flower and Kennett, (1996), who observed changes in $\delta^{18}O$ indicative of rapid East Antarctic Ice Sheet growth, and enhanced organic carbon burial with a maximum $\delta^{13}C$ reached at ~13.6 Ma (Shevenell et al., 2004; Holbourn et al., 2007). At the same time, we find evidence for a decline in SST of 3.4°C to a minimum of 33.3°C. The synchronous shifts in the $\delta^{13}C$ and $\delta^{18}O$ of benthic foraminifera are consistent with increased carbon burial during colder periods, thus feeding back into decreasing atmospheric CO_2, and supporting the hypothesis that the drawdown of atmospheric CO_2 can in part, be explained by enhanced export of organic carbon.

3.4 Late Miocene

The resolution of our data during the late Miocene is low, with a data gap from 12.5 to 9.2 Ma, and another gap between 6.5 and 5 Ma. We note the pCO_2 peak at ~9 Ma observed by Sosdian et al. (2018) is not seen in our record although this is likely due to the low resolution of our dataset. Between 8.8 and 6.5 Ma we find evidence for a decrease in atmospheric CO_2 of 205 µatm associated with a decrease in temperature of 3.1 °C.

3.5 CO_2 during Pliocene Warmth

Oxygen isotope data from a global benthic foraminiferal stack show that the Pliocene epoch (5.3-2.6 Ma) was initially characterized by warm conditions followed by the intensification of glaciation that occurred in several steps, including during MIS M2 (3.312-

3.264 Ma), followed by the Middle Pliocene Warm Period (Lisiecki and Raymo, 2005). Figure 5 shows that during the Early Pliocene warm interval, from 4.7 to 4.5 Ma, we calculate high pCO_2 values of 541 ± 124 ppm (2 SD, n=3, Table 3).

The Middle Pliocene Warm Period (MPWP – 3.29-2.97 Ma) is considered a relevant geological analogue for future climate change given ~3^{o}C warmer global temperatures and sea levels that were ~20 m higher than today (Dutton et al., 2015; Haywood et al., 2016), and is a target for model intercomparison projects, for which accurate paleo-atmospheric pCO_2 estimates are critical (Haywood et al., 2016). Our data support values of 515 ± 119 µatm (2 SD, n = 4) are consistent with previously published $\delta^{11}B$-derived pCO_2 from ODP Site 999 (Martinez-Boti et al., 2015b) but are higher than Bartoli et al. (2011), which was 320 ± 130 (2 SD, n=8) for Site 999, potentially due to instrument offset between N-TIMS and MC-ICP-MS (Martinez-Boti et al., 2015b). Our values are higher in comparison to boron isotope estimates from de La Vega et al. (2020) for Site 999 and calculations based on Martinez-Boti et al., (2015b.) This can suggest differences in air-sea equilibrium between sites. The pCO_2 trends in this study are similar to previous ones, the reconstructed pCO_2 show larger amplitude in our study. pCO_2 concentrations determined from ice cores from the early Pleistocene have recently been published (Yan et al., 2019, Figs. 4 and 5), and those values are in good agreement with our boron-derived pCO_2 at site 806/807 reported here, and with previous boron-based studies (Hönisch et al., 2009; Stap et al., 2016; Chalk et al., 2017).

3.6 Pliocene Glacial Intensification

The warmth and local pCO_2 maxima of the MPWP was followed by a strong decrease of temperature in upwelling and high latitude regions during from 3.3-2.7 Ma, coincident with glacial intensification in the Northern Hemisphere. This climate transition was hypothesized to be driven by the closure of the Panama seaway, the opening of the high latitudes and subsequent modifications of oceanic circulation. However, modeling from Lunt et al. (2008) supports an additional major role for CO_2 in the glaciation. pCO_2 thresholds have been proposed to explain the intensification of Northern Hemisphere Glaciation, with values proposed ranging from 280 µatm (DeConto et al., 2008) to 200 to 400 µatm (Koening et al., 2011).

From 3.3 to 3.0 Ma, our boron isotope-derived estimates of pCO_2 are typically 150 µatm higher than Bartoli et al. (2011), and de la Vega., (2020). This study, Martinez-Boti et

al. (2015b) and de la Vega et al., (2020) used an MC-ICP-MS so it is possible the differences reflect changes in air-sea equilibrium recorded at Site 999 compared to Sites 806/807.

The reconstruction for the WEP exhibits multiple steps during the decline in pCO_2, with a minimum observed at 4.42 Ma (360 ($\pm\frac{117}{85}$) µatm), at 3.45 Ma (323 ($\pm\frac{100}{75}$) µatm) and at 2.67 Ma (269 ($\pm\frac{77}{59}$) µatm) (Fig. 6). Those atmospheric CO_2 concentrations are consistent with the pCO_2 thresholds proposed by both DeConto et al. (2008) and Koening et al. (2011) for the intensification of Northern Hemisphere glaciation and the low CO_2 (280 ppmv) scenario from Lunt et al. (2008). We speculate that associated with Pliocene glacial intensification, at 4.42, 3.45 and 2.67 Ma, it is possible that the declines in CO_2 and ice growth in turn drove substantial changes in pole-to-equator temperature gradients and winds, that in turn may have impacted iron cycling (Watson et al., 2000; Robinson et al., 2005), stratification (Togweiller, 1999; Sigman et al., 2010), and other feedbacks that impact the amplitude of glacial/interglacial cycles and have been implicated as factors that could have contributed to Pliocene glacial intensification. Specifically, as the mean climate state of the planet became cooler, and glacial-interglacial cycles became larger in amplitude, enhanced windiness and dust transport and upwelling during glacials may have enhanced iron fertilization and subsequent carbon export. This could explain why glacial/interglacial amplitudes in WEP pCO_2 values decrease from the MPWP towards the Pleistocene, whereas variations in $\delta^{18}O$ are increasing.

3.7 Pleistocene

During the Pleistocene (2.58-0.01 Ma), the climate system experienced a transition in glacial/interglacial (G/I) variability from low amplitude, higher frequency and obliquity-dominated oscillations (i.e., ~ 41 kyr) of the late Pliocene to the high amplitude, lower frequency and eccentricity-dominated cycles (i.e.., ~100 kyr) of the last 800 kyr. This transition is termed the Middle Pleistocene Transition (0.8-1.2 Ma – MPT). Questions have been raised about the role of atmospheric CO_2 during this transition, including using boron-based proxies (Hönisch et al., 2009; Tripati et al., 2011; Chalk et al., 2017). Previous boron isotope studies have suggested that a decline in atmospheric CO_2 did not occur during the MPT (Hönisch et al., 2009, Chalk et al., 2017).

Although our pCO_2 results for the MPT (Fig. 9D) are broadly in the range of values reported by Hönisch et al. (2009) and Chalk et al. (2017), we have higher data coverage for

the middle and later part of the transition (Fig. 6). Taken alone, or when combined with the published data from Chalk et al. (2017) (that is also based on MC-ICPMS), our results support a reduction of both glacial and interglacial pCO_2 values. We also find evidence that during the MPT, glacial pCO_2 declined rapidly from 189 (±30) µatm at MIS 36 (Chalk et al., 2017) to reach a minimum of 164 ($\pm\frac{44}{35}$) µatm during MIS 30 and then remained relatively stable until the end of the MPT whereas interglacial pCO_2 values decrease gradually to reach post-MPT values.

In our record for the last 17 myr, the lowest pCO_2 is recorded at MIS 30 during the MPT, with values of 164 ($\pm\frac{44}{35}$) µatm, which supports an atmospheric CO_2 threshold that leads to ice sheet stability. During this transition, the pCO_2 threshold needed to build sufficiently large ice sheets that were able to survive the critical orbital phase of rising obliquity to ultimately switch to a 100 kyr world, was likely reached at MIS 30. The multiple feedbacks resulting from stable ice sheets (iron fertilization/productivity/changes in albedo/ changes in deep water formation) might have sustained larger mean global ice volumes over the subsequent 800 kyr. An asymmetrical decrease between pCO_2 values during interglacials relative to glacials, with glacials exhibiting the largest change across the MPT, would have led to increased sequestration of carbon during glacials in the 100 kyr world, as discussed by Chalk et al. (2017), with increased glacial dust input and iron fertilization.

3.8 Changes in volcanic activity and silicate weathering, and long-term pCO_2

On million-year timescales, atmospheric CO_2 is mainly controlled by volcanic activity and silicate weathering. Over the last 17 myr, two relative maxima in atmospheric pCO_2 are observed in our record, one during the MCO and a second around the late Miocene/early Pliocene (Fig. 7), though the timing for the latter is not precise due to a data gap for this period. The high CO_2 levels of the MCO are hypothesized (Foster et al., 2012) to coincide with increasing volcanic activity, associated with the eruption of the Columbia River Flood Basalts (Hooper et al., 2002; Kasbohm and Schoene, 2018), with recent geochronologic evidence published supporting higher eruption activity between 16.7 and 15.9 Ma (Kasbohm and Schoene, 2018). The second CO_2 peak could correspond to observed global increased volcanism in the early/middle Pliocene (Kennett and Thunell, 1977; Kroenke et al., 1993), and/or a change of silicate weathering regime. Strontium and lithium isotopes ($^{87/86}Sr$ and δ^7Li) have been used as proxy for silicate weathering activity. Although the strontium isotope

record exhibits a monotonous increase (Fig. 7), lithium isotope data (Misra and Froelich, 2012) are more variable with a transition from a period of increase seawater δ^7Li (e.g. non-steady state weathering) to stable seawater δ^7Li (e.g., steady state weathering) beginning at roughly 6.8 Ma (Fig. 7).

3.9 History of the WEP

The patterns observed in our study are also in line with major changes in the equatorial Pacific dynamic reported from other studies over these timescales (Figure 8). The development of the warm pool and transient changes between La Madre (La-Nina-like) to El Padre (El-Nino-like conditions) have been inferred from geological records (Nathan and Leckie, 2009), including foraminiferal assemblage data and asymmetric carbonate preservation between the west and the east equatorial Pacific (Chaisson and Ravelo, 2000; Nathan and Leckie, 2009), and sea surface and sub-surface temperature proxies (Wara et al, 2005; Rickaby and Halloran, 2005; Seki et al., 2012; Ford et al., 2012, 2015; Drury et al., 2018).

The increase in CO_2 in the late Miocene and early Pliocene in our record corresponds to the timing of the biogenic bloom in the Eastern equatorial Pacific that has been linked to a global biogenic bloom (Hermoyan and Owen, 2001). These blooms have been hypothesized to arise from an increase in nutrients (Hermoyan and Owen, 2001) that arose due to higher rates of weathering as well as change in oceanic circulation due to Indonesian and Central American Seaways constrictions (Gupta and Thomas, 1999; Grant and Dickens, 2002 amongst many others). The change in silicate weathering regime inferred from the record of δ^7Li (Misra and Froelich, 2012) would also be consistent with this hypothesis.

3.9 Outlook

This study is the first to report a long-term pCO_2 record for the WEP derived from boron isotopes. Using samples from ODP Sites 806 and 807, we build on past efforts to reconstruct atmospheric pCO_2 from carbon isotopes in marine organic matter (Rayno et al., 1996), alkenones (Pagani et al., 2010), and B/Ca (Tripati et al., 2009, 2011), all of which have been shown to have a number of complexities and potential sources of systematic error (e.g., Tripati et al., 2011). It also builds on efforts using boron isotopes in other regions using MC-ICP-MS (Seki et al., 2010; Foster et al., 2012, 2014; Greenop et al., 2014; Martinez-Boti et al., 2015b; Stap et al., 2016; Chalk et al., 2017; de la Vega et al., 2020). Future constraints

on the vertical structure of the WEP during these transitions will potentially be illuminating. Comparison to records from different parts of the ocean will also help us better understand how air-sea disequilibria has changed through time.

4. Conclusions

[1] We developed a reconstruction of atmospheric pCO_2 based on $\delta^{11}B$ of planktic foraminifera from Sites 806 and 807 located in the Western Equatorial Pacific for the Miocene to Recent. The record is at present the most data-rich and continuous boron-isotope reconstruction in the literature for a single region over the last 20 myrs, with variable resolution that captures both long-term and short-term variability associated with several key transitions.

[2] As expected, these data reproduce the pCO_2 record from ice cores, consistent with the sites being in equilibrium with the atmosphere.

[3] The MCO has higher pCO_2 than reconstructions from other sites, with values estimated as 479 ± 173 µatm (2 SD, n=4), potentially linked to the eruption of the Columbia River Flood Basalts, with values declining into the early Pliocene.

[4] Major drops in pCO_2 occurred at 12.9, 4.42, 3.45 and 2.71 Ma, including during Pliocene glacial intensification.

[5] We find support for a larger reduction in glacial pCO_2 during the MPT compared to interglacial pCO_2, and a minimum in pCO_2 during glacial MIS 30. These findings support a role for CO_2 in the transition from a 41 kyr to a 100 kyr world.

[6] Higher-resolution boron isotope records from the WEP will allow for further testing of these findings. Additional constraints on temperature, such as from clumped isotopes in the WEP (Tripati et al., 2014), could allow for uncertainties in pCO_2 estimates from boron isotopes to be reduced.

Acknowledgments

The authors wish to thank the Tripati Lab, including Lea Bonnin, and Alexandra Villa, for assistance with picking samples; the IODP repository for provision of samples; Mervyn Greaves for technical support and use of laboratory space at the University of Cambridge; Yoan Germain, Emmanuel Ponzevera, Céline Liorzou and Oanez Lebeau for technical support and use of laboratory space at IUEM and Ifremer (Plouzané, France).

Financial support

This research is supported by DOE BES grant no. DE-FG02-13ER16402 to AKT, by the International Research Chair Program that is funded by the French government (LabexMer ANR-10-LABX-19-01) to AKT and RAE, and IAGC student research grant 2017.

6. References

Aggarwal, S. K., & You, C. F.: A review on the determination of isotope ratios of boron with mass spectrometry. Mass Spectrometry Reviews, 36(4), 499-519, 2017.

Allen, K. A. and Hönisch, B.: The planktic foraminiferal B/Ca proxy for seawater carbonate chemistry, A critical evaluation, Earth Planet. Sci. Lett, 345–348, 203–211, 2012.

Allen, K. A., Hönisch, B., Eggins, S. M., Yu, J., Spero, H. J., Elderfield, H.: Controls on boron incorporation in cultured tests of the planktic foraminifer Orbulina universa. Earth and Planetary Science Letters, 309(3-4), 291-301, 2011.

Anagnostou, E., John, E. H., Edgar, K. M., Foster, G. L., Ridgwell, A., Inglis, G. N., D. Pancost, R., J. Lunt, D., Pearson, P. N.: Changing atmospheric CO2 concentration was the primary driver of early Cenozoic climate. Nature, 533(7603), 380-384, 2016.

Babila, T., Huang, K. F., Rosenthal, Y., Conte, M. H., & Lin, H. L. Development of B/Ca as a seawater pH proxy using sediment trap time series, abstract, 2010.

Badger M. P. S., Chalk T. B., Foster G. L., Bown P. R., Gibbs S. J., Sexton P. F., Schmidt D. N., Pälike H., Mackensen A. and Pancost R. D.: Insensitivity of alkenone carbon isotopes to atmospheric CO2 at low to moderate CO2 levels. Climate of the Past, 15(2), 539-554, 2019.

Badger M. P. S., Lear C. H., Pancost R. D., Foster G. L., Bailey T. R., Leng M. J. and Abels H. A.: CO2 drawdown following the middle Miocene expansion of the Antarctic Ice Sheet. Paleoceanography 28, 42–53, 2013.

Barker S., Greaves M. and Elderfield H.: A study of cleaning procedures used for foraminiferal Mg/Ca paleothermometry. Geochemistry, Geophys. Geosystems 4, 1–20, 2003.

Bartoli G., Hönisch B. and Zeebe R. E.: Atmospheric CO2 decline during the Pliocene intensification of Northern Hemisphere glaciations. Paleoceanography 26, 1–14, 2011.

Berger, W.H., Kroenke, J.W., Mayer, L.A.: Proceedings of the Ocean Drilling Program, Scientific Results, Vol. 130, 1993.

Berger, W.H., Kroenke, L., Janecek, T.R., et al., . Proceedings of the Ocean Drilling Program. Initial Reports, p. 130, 1991.

Bian, N., & Martin, P. A.: Investigating the fidelity of Mg/Ca and other elemental data from reductively cleaned planktonic foraminifera. Paleoceanography, 25(2), 2010.

Bolton C. T. and Stoll H. M.: Late Miocene threshold response of marine algae to carbon dioxide limitation. Nature 500, 558–562, 2013.

Bolton C. T., Hernández-Sánchez M. T., Fuertes M.-Á., González-Lemos S., Abrevaya L., Mendez-Vicente A., Flores J.-A., Probert I., Giosan L., Johnson J. and Stoll H. M. : Decrease in coccolithophore calcification and CO2 since the middle Miocene. Nat. Commun. 7, 10284, 2016.

Boyer, T.P., J. I. Antonov, O. K. Baranova, C. Coleman, H. E. Garcia, A. Grodsky, D. R. Johnson, R. A. Locarnini, A. V. Mishonov, T.D. O'Brien, C.R. Paver, J.R. Reagan, D. Seidov, I. V. Smolyar, and M. M. Zweng, 2013: World Ocean Database 2013, NOAA

Atlas NESDIS 72, S. Levitus, Ed., A. Mishonov, Technical Ed.; Silver Spring, MD, 209 pp., http://doi.org/10.7289/V5NZ85MT, 2013.
Brennan, S. T., Lowenstein, T. K., & Cendón, D. I. : The major-ion composition of Cenozoic seawater: The past 36 million years from fluid inclusions in marine halite. American Journal of Science, 313(8), 713-775, 2013.
Caves J. K., Jost A. B., Lau K. V. and Maher K.: Cenozoic carbon cycle imbalances and a variable weathering feedback. Earth Planet. Sci. Lett. 450, 152–163, 2016.
Chalk T. B., Hain M. P., Foster G. L., Rohling E. J., Sexton P. F., Badger M. P. S., Cherry S. G., Hasenfratz A. P., Haug G. H., Jaccard S. L., Martínez-García A., Pälike H., Pancost R. D. and Wilson P. A.: Causes of ice age intensification across the Mid-Pleistocene Transition. Proc. Natl. Acad. Sci., 201702143, 2017.
Coggon R. M., Teagle D. A. H. and Dunkley Jones T. Comment on "What do we know about the evolution of Mg to Ca ratios in seawater?" by Wally Broecker and Jimin Yu. Paleoceanography 26, 2011.
DeConto, R. M., & Pollard, D.: Rapid Cenozoic glaciation of Antarctica induced by declining atmospheric CO2. Nature, 421(6920), 245-249, 2003.
DeConto R. M., Pollard D., Wilson P. A., Pälike H., Lear C. H. and Pagani M.: Thresholds for Cenozoic bipolar glaciation. Nature 455, 652–656, 2008.
DeFantle M. S. and DePaolo D. J.: Sr isotopes and pore fluid chemistry in carbonate sediment of the Ontong Java Plateau: Calcite recrystallization rates and evidence for a rapid rise in seawater Mg over the last 10 million years. Geochim. Cosmochim. Acta 70, 3883–3904, 2006.
Dekens P. S., Lea D. W., Pak D. K. and Spero H. J.: Core top calibration of Mg/Ca in tropical foraminifera: Refining paleotemperature estimation. Geochemistry, Geophys. Geosystems 3, 1–29, 2002.
Delaney, M. L., Bé, A. W., & Boyle, E. A.: Li, Sr, Mg, and Na in foraminiferal calcite shells from laboratory culture, sediment traps, and sediment cores. Geochimica et Cosmochimica Acta, 49(6), 1327-1341, 1985.
de la Vega, E., Chalk, T. B., Wilson, P. A., Bysani, R. P., & Foster, G. L.: Atmospheric CO2 during the Mid-Piacenzian Warm Period and the M2 glaciation. Scientific Reports, 10(1), 1-8, 2020.
Dickson A. G.: Thermodynamics of the Dissociation of Boric Acid in Potassium Chloride Solutions from 273.15 to 318.15 K. J. Chem. Eng. Data 35, 253–257, 1990.
Drury, A. J., Lee, G. P., Gray, W. R., Lyle, M., Westerhold, T., Shevenell, A. E., & John, C. M.: Deciphering the state of the late Miocene to early Pliocene equatorial Pacific. Paleoceanography and paleoclimatology, 33(3), 246-263, 2018.
Evans, D. & Müller, W.: Deep time foraminifera Mg/Ca paleothermometry: Nonlinear correction for secular change in seawater Mg/Ca. Paleoceanography 27, PA4205, 2012.
Evans, D., Wade, B. S., Henenhan, M., Erez, J., & Müller, W.: Revisiting carbonate chemistry controls on planktic foraminifera Mg/Ca: implications for sea surface temperature and hydrology shifts over the Paleocene–Eocene Thermal Maximum and Eocene–Oligocene transition. Climate of the Past, 12(4), 819-835, 2016.
Farmer, J. R., Hönisch, B., & Uchikawa, J.: Single laboratory comparison of MC-ICP-MS and N-TIMS boron isotope analyses in marine carbonates. Chemical Geology, 447, 173-182, 2016.
Farrell, J.W., Raffi, I., Janecek, T.,Murray, D.W., Levitan,M., Dadey, K.A., Emeis, K.C., Lyle, M., Flores, J.A., Hovan, S: Late Neogene sedimentation patterns in the eastern Equatorial Pacific Ocean. In: Pisias,N.G.,Mayer, L.A., Janecek, T.R., Palmer-Julson, A.,

van Andel, T.H. (Eds.), Proceedings of the Ocean Drilling Program. Scientific Results, vol. 138. ocean Drilling Program, College Station, TX, pp. 717–756, 1995.
Flower, B. P., & Kennett, J. P.: Middle Miocene deepwater paleoceanography in the southwest Pacific: relations with East Antarctic Ice Sheet development. Oceanographic Literature Review, 8(43), 796, 1996.
Ford, H. L., Ravelo, A. C., Dekens, P. S., LaRiviere, J. P., & Wara, M. W.: The evolution of the equatorial thermocline and the early Pliocene El Padre mean state. Geophysical Research Letters, 42(12), 4878-4887, 2015.
Foster G. L.: Seawater pH, pCO2and [CO2-3] variations in the Caribbean Sea over the last 130 kyr: A boron isotope and B/Ca study of planktic foraminifera. Earth Planet. Sci. Lett. 271, 254–266, 2008.
Foster G. L. and Rohling E. J.: Relationship between sea level and climate forcing by CO2 on geological timescales. Proc. Natl. Acad. Sci. 110, 1209–1214, 2013.
Foster G. L. and Sexton P. F.: Enhanced carbon dioxide outgassing from the eastern equatorial Atlantic during the last glacial. Geology 42, 1003–1006, 2014.
Foster, G. L., Hönisch, B., Paris, G., Dwyer, G. S., Rae, J. W., Elliott, T., Gaillardet, J., Hemming, N. G., Louvat, P., Vengosh, A.: Interlaboratory comparison of boron isotope analyses of boric acid, seawater and marine CaCO3 by MC-ICPMS and NTIMS. Chemical Geology, 358, 1-14, 2013.
Foster G. L., Lear C. H. and Rae J. W. B.: The evolution of pCO2, ice volume and climate during the middle Miocene. Earth Planet. Sci. Lett. 341–344, 243–254, 2012.
Foster G. L., Royer D. L. and Lunt D. J.: Future climate forcing potentially without precedent in the last 420 million years. Nat. Commun. 8, 14845. http://dx.doi.org/10.1038/ncomms14845, 2017.
Gasson E., DeConto R. M., Pollard D. and Levy R. H.: Dynamic Antarctic ice sheet during the early to mid-Miocene. Proc. Natl. Acad. Sci. 113, 3459–3464, 2016.
Gothmann A. M., Stolarski J., Adkins J. F., Schoene B., Dennis K. J., Schrag D. P., Mazur M. and Bender M. L.: Fossil corals as an archive of secular variations in seawater chemistry since the Mesozoic. Geochim. Cosmochim. Acta 160, 188–208, 2015.
GraphPad Prism version 7.00 for Windows, GraphPad Software, La Jolla California USA, www.graphpad.com"
Gray, W. R., & Evans, D.: Nonthermal influences on Mg/Ca in planktonic foraminifera: a review of culture studies and application to the Last Glacial Maximum. Paleoceanography and Paleoclimatology, 34(3), 306-315, 2019.
Gray, W. R., Weldeab, S., Lea, D. W., Rosenthal, Y., Gruber, N., Donner, B., & Fischer, G.: The effects of temperature, salinity, and the carbonate system on Mg/Ca in Globigerinoides ruber (white): A global sediment trap calibration. Earth and Planetary Science Letters, 482, 607-620, 2018.
Greenop R., Foster G. L., Wilson P. A. and Lear C. H.: Middle Miocene climate instability associated with high-amplitude CO2 variability. Paleoceanography 29, 845–853, 2014.
Greenop R., Hain M. P., Sosdian S. M., Oliver K. I. C., Goodwin P., Chalk T. B., Lear C. H., Wilson P. A. and Foster G. L.: A record of Neogene seawater δ11B reconstructed from paired δ11B analyses on benthic and planktic foraminifera. Clim. Past 13, 149–170, 2017.
Guillermic, M., Misra, S., Eagle, R., Villa, A., Chang, F., Tripati, A.,: Seawater pH reconstruction using boron isotopes in multiple planktonic foraminifera species with different depth habitats and their potential to constrain pH and pCO2 gradients. Biogeosciences, 17(13), 3487-3510, 2020.

Gutjahr, M., Bordier, L., Douville, E., Farmer, J., Foster, G. L., Hathorne, E., Hönish, B., Lemarchand, D., Louvat, P., McCulloch, M., Noireaux, J., Pallavicini, N., Rodushkin, I., Roux, P., Stewart, J., Thil, F. You, C.F., Boron Isotope Intercomparison Project (BIIP): Development of a new carbonate standard for stable isotopic analyses. In EGU general assembly conference abstracts, Vol. 16, 2014.

Hansen, J., Sato, M., & Ruedy, R.: Perception of climate change. Proceedings of the National Academy of Sciences, 109(37), 2012.

Hansen J., Sato M., Russell G. and Kharecha P.: Climate sensitivity, sea level and atmospheric carbon dioxide. Philos. Trans. R. Soc. A Math. Phys. Eng. Sci. 371, 1–38, 2013.

Haywood, A. M., Dowsett, H. J., & Dolan, A. M.: Integrating geological archives and climate models for the mid-Pliocene warm period. Nature communications, 7(1), 1-14, 2016.

Hemming N. G. and Hanson G. N.: Boron isotopic composition and concentration in modern marine carbonates. Geochim. Cosmochim. Acta 56, 537–543, 1992.

Henehan M. J., Foster G. L., Bostock H. C., Greenop R., Marshall B. J. and Wilson P. A.: A new boron isotope-pH calibration for Orbulina universa, with implications for understanding and accounting for 'vital effects.' Earth Planet. Sci. Lett. 454, 282–292, 2016.

Henehan M. J., Rae J. W. B., Foster G. L., Erez J., Prentice K. C., Kucera M., Bostock H. C., Martínez-Botí M. A., Milton J. A., Wilson P. A., Marshall B. J. and Elliott T. (2013) Calibration of the boron isotope proxy in the planktonic foraminifera Globigerinoides ruber for use in palaeo-CO2reconstruction. Earth Planet. Sci. Lett. 364, 111–122, 2013.

Higgins J. A., Kurbatov A. V, Spaulding N. E., Brook E., Introne D. S., Chimiak L. M., Yan Y., Mayewski P. A. and Bender M. L.: Atmospheric composition 1 million years ago from blue ice in the Allan Hills, Antarctica. Proc. Natl. Acad. Sci. 112, 6887–6891, 2015.

Holbourn A., Kuhnt W., Frank M. and Haley B. A.: Changes in Pacific Ocean circulation following the Miocene onset of permanent Antarctic ice cover. Earth Planet. Sci. Lett. 365, 38–50, 2013.

Holcomb M., DeCarlo T. M., Schoepf V., Dissard D., Tanaka K. and McCulloch M.: Cleaning and pre-treatment procedures for biogenic and synthetic calcium carbonate powders for determination of elemental and boron isotopic compositions. Chem. Geol. 398, 11–21, 2015.

Hönisch, B. and Hemming, N. G., Ground-truthing the boron isotope-paleo-pH proxy in planktonic foraminifera shells: Partial dissolution and shell size effects, Paleoceanography 19, 1–13, 2004.

Honisch, B., Allen, K. A., Lea, D. W., Spero, H. J., Eggins, S. M., Arbuszewski, J., deMenocal, P., Rosenthal, Y., D. Russel, a.: Elderfield, H.: The influence of salinity on Mg/Ca in planktic foraminifers–Evidence from cultures, core-top sediments and complementary d 18 O. Geochimica Et Cosmochimica Acta, 121, 196-213, 2013.

Hönisch, B., Eggins, S. M., Haynes, L. L., Allen, K. A., Holland, K. D., & Lorbacher, K.: Boron Proxies in Paleoceanography and Paleoclimatology. John Wiley & Sons, 2019.

Hönisch B., Hemming N. G., Archer D., Siddall M. and McManus J. F.: Atmospheric carbon dioxide concentration across the mid-pleistocene transition. Science 324, 1551–1554, 2009.

Horita J., Zimmermann H. and Holland H. D.: Chemical evolution of seawater during the Phanerozoic: Implications from the record of marine evaporites. Geochim. Cosmochim. Acta 66, 3733–3756., 2002.

IPCC: Climate Change 2014 - The Physical Science Basis, edited by Intergovernmental Panel on Climate Change, Cambridge University Press, Cambridge., 2014.
IPCC: Global Warming of 1.5 ºC- edited by Intergovernmental Panel on Climate Change, 2018.
Johnstone, H. J., Lee, W., & Schulz, M.: Effect of preservation state of planktonic foraminifera tests on the decrease in Mg/Ca due to reductive cleaning and on sample loss during cleaning. Chemical Geology, 420, 23-36, 2016.
Kasbohm, J., & Schoene, B.: Rapid eruption of the Columbia River flood basalt and correlation with the mid-Miocene climate optimum. Science advances, 4(9), eaat8223, 2018.
Kennett, J. P., & Thunell, R. C.: On explosive Cenozoic volcanism and climatic implications. Science, 196(4295), 1231-1234, 1977.
Kısakürek, B., Eisenhauer, A., Böhm, F., Garbe-Schönberg, D., & Erez, J.: Controls on shell Mg/Ca and Sr/Ca in cultured planktonic foraminiferan, Globigerinoides ruber (white). Earth and Planetary Science Letters, 273(3-4), 260-269, 2008.
Klochko K., Kaufman A. J., Yao W., Byrne R. H. and Tossell J. A.: Experimental measurement of boron isotope fractionation in seawater. Earth Planet. Sci. Lett. 248, 261–270, 2006.
Koenig S. J., DeConto R. M. and Pollard D.: Late Pliocene to Pleistocene sensitivity of the Greenland Ice Sheet in response to external forcing and internal feedbacks. Clim. Dyn. 37, 1247–1268, 2011.
Kroenke, L. W., Berger, W. H., Janecek, T. R. and Shipboard Scientific Party: Proceedings of the Ocean Drilling Program, Initial Reports, Vol. 130, 1991.
Lea, D. W.: The 100 000-yr cycle in tropical SST, greenhouse forcing, and climate sensitivity. Journal of Climate, 17(11), 2170-2179, 2004.
Lee, K., Kim, T. W., Byrne, R. H., Millero, F. J., Feely, R. A., & Liu, Y. M.: The universal ratio of boron to chlorinity for the North Pacific and North Atlantic oceans. Geochimica et Cosmochimica Acta, 74(6), 1801-1811, 2010.
Lea, D. W., Pak, D. K., & Spero, H. J.: Climate impact of late Quaternary equatorial Pacific sea surface temperature variations. Science, 289(5485), 1719-1724, 2000.
Lemarchand D., Gaillardet J., Lewin and Allégre C. J.: The influence of rivers on marine boron isotopes and implications for reconstructing past ocean pH. Nature 408, 951–954, 2000.
Lisiecki L. E. and Raymo M. E.: A Pliocene-Pleistocene stack of 57 globally distributed benthic δ18O records. Paleoceanography 20, 1–17, 2005.
Lloyd, N. S., Sadekov, A. Y. and Misra, S., Application of 1013ohm Faraday cup current amplifiers for boron isotopic analyses by solution mode and laser ablation multicollector inductively coupled plasma mass spectrometry, Rapid Commun. Mass Spectrom., 32, 9–18, 2018.
Lueker, T. J., Dickson, A. G., & Keeling, C. D.: Ocean pCO2 calculated from dissolved inorganic carbon, alkalinity, and equations for K1 and K2: validation based on laboratory measurements of CO2 in gas and seawater at equilibrium. Marine chemistry, 70(1-3), 105-119, 2000.
Lunt D. J., Foster G. L., Haywood A. M. and Stone E. J.: Late Pliocene Greenland glaciation controlled by a decline in atmospheric CO2levels. Nature 454, 1102–1105, 2008.
Lunt, D. J., Haywood, A. M., Schmidt, G. A., Salzmann, U., Valdes, P. J., & Dowsett, H. J.: Earth system sensitivity inferred from Pliocene modelling and data. Nature Geoscience, 3(1), 60-64, 2010.

Lüthi D., Le Floch M., Bereiter B., Blunier T., Barnola J. M., Siegenthaler U., Raynaud D., Jouzel J., Fischer H., Kawamura K. and Stocker T. F.: High-resolution carbon dioxide concentration record 650,000-800,000 years before present. Nature 453, 379–382, 2008.

Martínez-Botí, M. A., Marino G., Foster G. L., Ziveri P., Henehan M. J., Rae J. W. B., Mortyn P. G. and Vance D.: Boron isotope evidence for oceanic carbon dioxide leakage during the last deglaciation. Nature 518, 219–222, 2015.

Mavromatis, V., Montouillout, V., Noireaux, J., Gaillardet, J. and Schott, J., Characterization of boron incorporation and speciation in calcite and aragonite from co-precipitation experiments under controlled pH, temperature and precipitation rate, Geochim. Cosmochim. Acta, 150, 299–313, 2015.

McCulloch M. T., Holcomb M., Rankenburg K. and Trotter J. A.: Rapid, high-precision measurements of boron isotopic compositions in marine carbonates. Rapid Commun. Mass Spectrom. 28, 2704–2712, 2014.

Medina-Elizalde M. and Lea D. W.: The mid-pleistocene transition in the tropical pacific. Science 310, 1009–1012, 2005.

Misra, S. and Froelich, P. N.: Lithium isotope history of cenozoic seawater: Changes in silicate weathering and reverse weathering. Science (80-.). 335, 818–823, 2012.

Misra, S., Greaves, M., Owen, R., Kerr, J., Elmore, A. C. and Elderfield, H.: Determination of B/Ca of natural carbonates by HR-ICP-MS. Geochemistry, Geophys. Geosystems 15, 1617–1628, 2014a.

Misra, S., Owen, R., Kerr, J., Greaves, M. and Elderfield, H.: Determination of δ11B by HR-ICP-MS from mass limited samples: Application to natural carbonates and water samples. Geochim. Cosmochim. Acta 140, 531–552, 2014b.

Nathan, S. A., & Leckie, R. M.: Palaeogeography, Palaeoclimatology, Palaeoecology, 274(3-4), 140-159, 2009.

Ni Y., Foster G. L., Bailey T., Elliott T., Schmidt D. N., Pearson P., Haley B. and Coath C.: A core top assessment of proxies for the ocean carbonate system in surface-dwelling foraminifers. Paleoceanography 22, 2007.

Nir O., Vengosh A., Harkness J. S., Dwyer G. S. and Lahav O.: Direct measurement of the boron isotope fractionation factor: Reducing the uncertainty in reconstructing ocean paleo-pH. Earth Planet. Sci. Lett. 414, 1–5, 2015.

Nürnberg, D., Bijma, J., & Hemleben, C.: Assessing the reliability of magnesium in foraminiferal calcite as a proxy for water mass temperatures. Geochimica et Cosmochimica Acta, 60(5), 803-814, 1996.

O'Brien C. L., Foster G. L., Martínez-Botí M. A., Abell R., Rae J. W. B. and Pancost R. D.: High sea surface temperatures in tropical warm pools during the Pliocene. Nat. Geosci. 7, 606–611, 2014.

Osborne, E. B., Umling, N. E., Bizimis, M., Buckley, W., Sadekov, A., Tappa, E., Marshall, B., R. Sautter, L., Thunell, R. C.: A Sediment Trap Evaluation of B/Ca as a Carbonate System Proxy in Asymbiotic and Nondinoflagellate Hosting Planktonic Foraminifera. Paleoceanography and Paleoclimatology, 35(2), 2020.

Pagani P., Freeman G., Arthur F., Schuster M., Tiercelin J.-J. and Brunet M.: Late miocene atmospheric CO(2) concentrations and the expansion of C(4) grasses. Science 285, 876–9, 1999.

Pagani M., Liu Z., Lariviere J. and Ravelo A. C.: High Earth-system climate sensitivity determined from Pliocene carbon dioxide concentrations. Nat. Geosci. 3, 27–30, 2010.

Pagani M., Zachos J. C., Freeman K. H., Tipple B. and Bohaty S.: Atmospheric science: Marked decline in atmospheric carbon dioxide concentrations during the Paleogene. Science 309, 600–603, 2005.

Pearson, P. N., & Palmer, M. R.: Atmospheric carbon dioxide concentrations over the past 60 million years. *Nature*, *406*(6797), 695-699, 2000.
Perez, F. F., & Fraga, F.: Association constant of fluoride and hydrogen ions in seawater. Marine Chemistry, 21(2), 161-168, 1987.
Petit J. R., Jouzel J., Raynaud D., Barkov N. I., Barnola J. M., Basile I., Bender M., Chappellaz J., Davis M., Delaygue G., Delmotte M., Kotiyakov V. M., Legrand M., Lipenkov V. Y., Lorius C., Pépin L., Ritz C., Saltzman E. and Stievenard M.: Climate and atmospheric history of the past 420,000 years from the Vostok ice core, Antarctica. Nature 399, 429–436, 1999.
Pierrot, D., Lewis, E., & Wallace, D. W. R.: MS Excel program developed for CO2 system calculations. ORNL/CDIAC-105a. Carbon Dioxide Information Analysis Center, Oak Ridge National Laboratory, US Department of Energy, Oak Ridge, Tennessee, 10, 2006.
Raitzsch M. and Hönisch B.: Cenozoic boron isotope variations in benthic foraminifers. Geology 41, 591–594, 2013.
Raitzsch M., Bijma J., Benthien A., Richter K. U., Steinhoefel G. and Kučera M.: Boron isotope-based seasonal paleo-pH reconstruction for the Southeast Atlantic – A multispecies approach using habitat preference of planktonic foraminifera. Earth Planet. Sci. Lett. 487, 138–150, 2018.
Ravelo, A. C., Lawrence, K. T., Fedorov, A., & Ford, H. L.: Comment on "A 12-million-year temperature history of the tropical Pacific Ocean". Science, 346(6216), 1467-1467, 2014.
Retallack G. J.: Greenhouse crises of the past 300 million years. Geol. Soc. Am. Bull. 121, 1441–1455, 2009.
Rickaby, R. E. M. and Halloran, P.: Cool La Nina During the Warmth of the Pliocene?, Science, 307, 1948–1952, 2005.
Ridgwell A. and Zeebe R. E.: The role of the global carbonate cycle in the regulation and evolution of the Earth system. Earth Planet. Sci. Lett. 234, 299–315, 2005.
Royer D. L.: Stomatal density and stomatal index as indicators of paleoatmospheric CO2 concentration. Rev. Palaeobot. Palynol. 114, 1–28, 2001.
Russell, A. D., Hönisch, B., Spero, H. J., & Lea, D. W.: Effects of seawater carbonate ion concentration and temperature on shell U, Mg, and Sr in cultured planktonic foraminifera. Geochimica et Cosmochimica Acta, 68(21), 4347-4361, 2004.
Schmittner, A., Urban, N. M., Shakun, J. D., Mahowald, N. M., Clark, P. U., Bartlein, P. J., ... & Rosell-Melé, A. (2011). Climate sensitivity estimated from temperature reconstructions of the Last Glacial Maximum. *Science*, *334*(6061), 1385-1388.
Seki O., Foster G. L., Schmidt D. N., Mackensen A., Kawamura K. and Pancost R. D.: Alkenone and boron-based Pliocene pCO2records. Earth Planet. Sci. Lett. 292, 201–211, 2010.
Shackleton N.J. , Berger A., Peltier W.R,: Trans. R. Soc. Edinb. Earth Sci. 81, 251. Shipboard Leg, O. D. P., Map, O. D. P., & Map, D. S. D.: P. Initial Reports: Volume 130. doi:10.2973/odp.proc.ir.130.108.1991, 1991.
Shevenell, A. E., Kennett, J. P., & Lea, D. W.: Middle Miocene southern ocean cooling and Antarctic cryosphere expansion. *Science*, *305*(5691), 1766-1770, 2004.
Shlitzer, R., Ocean Data View, https://odv.awi.de, 2016.
Siegenthaler, U., Stocker, T. F., Monnin, E., Lüthi, D., Schwander, J., Stauffer, B, Raynaud, D., Barnola, JM., Fischer, H., Masson-Delmotte, V., Jouzel, J.: Stable carbon cycle–climate relationship during the late Pleistocene. Science, 310(5752), 1313-1317, 2005.

Sosdian, S. M., Greenop R., Hain M. P., Foster G. L., Pearson P. N. and Lear C. H.: Constraining the evolution of Neogene ocean carbonate chemistry using the boron isotope pH proxy. Earth Planet. Sci. Lett. 498, 362–376, 2018.

Stap L. B., de Boer B., Ziegler M., Bintanja R., Lourens L. J. and van de Wal R. S. W.: CO2over the past 5 million years: Continuous simulation and new δ11B-based proxy data. Earth Planet. Sci. Lett. 439, 1–10, 2016.

Sutton J. N., Liu Y.-W., Ries J. B., Guillermic M., Ponzevera E. and Eagle R. A.: δ11B as monitor of calcification site pH in divergent marine calcifying organisms. Biogeosciences 15, 1447–1467, 2018.

Takahashi T., Sutherland S. C., Chipman D. W., Goddard J. G. and Ho C.: Climatological distributions of pH, pCO2, total CO2, alkalinity, and CaCO3saturation in the global surface ocean, and temporal changes at selected locations. Mar. Chem. 164, 95–125, 2014.

Tan, N., Ramstein, G., Dumas, C., Contoux, C., Ladant, J. B., Sepulchre, P., Zhang, Z., De Schepper, S.: Exploring the MIS M2 glaciation occurring during a warm and high atmospheric CO2 Pliocene background climate. Earth and Planetary Science Letters, 472, 266-276, 2017.

Tierney, J. E., Zhu, J., King, J., Malevich, S. B., Hakim, G. J., & Poulsen, C. J. (2020). Glacial cooling and climate sensitivity revisited. *Nature*, *584*(7822), 569-573.

Thomas, E.: Descent into the Icehouse. Geology 36, 191–192, 2008.

Tripati, A., & Darby, D.: Evidence for ephemeral middle Eocene to early Oligocene Greenland glacial ice and pan-Arctic sea ice. Nature communications, 9(1), 1-11, 2018

Tripati A. K., Roberts C. D. and Eagle R. A.: Coupling of CO2and Ice sheet stability over major climate transitions of the last 20 million years. Science (80-.). 326, 1394–1397, 2009.

Tripati A. K., Roberts C. D., Eagle R. A. and Li G.: A 20 million year record of planktic foraminiferal B/Ca ratios: Systematics and uncertainties in pCO2reconstructions. Geochim. Cosmochim. Acta 75, 2582–2610. http://dx.doi.org/10.1016/j.gca.2011.01.018, 2011.

Tyrrell, T., & Zeebe, R. E.: History of carbonate ion concentration over the last 100 million years. Geochimica et Cosmochimica Acta, 68(17), 3521-3530, 2004.

Van Der Burgh J., Visscher H., Dilcher D. L. and Kürschner W. M.: Paleoatmospheric signatures in Neogene fossil leaves. Science 260, 1788–1790, 1993.

Vogl J. and Rosner M.: Production and Certification of a Unique Set of Isotope and Delta Reference Materials for Boron Isotope Determination in Geochemical, Environmental and Industrial Materials. Geostand. Geoanalytical Res. 36, 161–175, 2012.

Wara M. W., Ravelo A. C. and Delaney M. L.: Climate change: Permanent El Niño-like conditions during the Pliocene warm period. Science 309, 758–761, 2005.

Yan, Y., Bender, M. L., Brook, E. J., Clifford, H. M., Kemeny, P. C., Kurbatov, A. V., Mackay, S., Mayewski, P.A., Ng, J., Severinghaus, J.P., Higgins, J. A.: Two-million-year-old snapshots of atmospheric gases from Antarctic ice. Nature, 574(7780), 663-666, 2019.

Yu, J., Elderfield, H., Greaves, M., & Day, J.: Preferential dissolution of benthic foraminiferal calcite during laboratory reductive cleaning. Geochemistry, Geophysics, Geosystems, 8(6), 2007a.

Yu J., Elderfield H. and Hönisch B.: B/Ca in planktonic foraminifera as a proxy for surface seawater pH. Paleoceanography 22, 2007.

Zachos J. C., Dickens G. R. and Zeebe R. E.: An early Cenozoic perspective on greenhouse warming and carbon-cycle dynamics. Nature 451, 279–283, 2008.

Zachos, J., Pagani, M., Sloan, L., Thomas, E., & Billups, K.: Trends, rhythms, and aberrations in global climate 65 Ma to present. science, 292(5517), 686-693, 2001.
Zeebe R. E. and Wolf-Gladrow D.: CO2 in Seawater: Equilibrium, Kinetics, Isotopes Elsevier Oceanography Series 65, Amsterdam, 2001.
Zhang Y. G., Pagani M., Liu Z., Bohaty S. M. and Deconto R.: A 40-million-year history of atmospheric CO2. Philos. Trans. R. Soc. A Math. Phys. Eng. Sci. 371, 20130096–20130096, 2013.
Zhang, Y. G., Pagani, M., & Liu, Z.: A 12-million-year temperature history of the tropical Pacific Ocean. *Science*, *344*(6179), 84-87, 2014.
Zhang, J., Wang, P., Li, Q., Cheng, X., Jin, H., & Zhang, S.: Western equatorial Pacific productivity and carbonate dissolution over the last 550 kyr: Foraminiferal and nannofossil evidence from ODP Hole 807A. Marine Micropaleontology, 64(3-4), 121-140, 2007.

Figure caption

Figure 1: A. Map of air-sea pCO_2 (ΔpCO_2, µatm, data from Takahashi et al., 2014 and map realized on Ocean Data view, Shlitzer, 2016) showing the location of ODP Sites 806 and 807 (black circles). Depth profiles for preindustrial parameters, **B.** pH calculated from GLODAP database and corrected from anthropogenic inputs, **C.** boron isotopic composition of borate ion ($\delta^{11}B_{borate}$) with associated propagated uncertainties.

Figure 2: Reconstruction of surface pCO_2 for the past 0.8 My from *T. sacculifer* at ODP Sites 806 and 807. This plot compares pCO_2 from boron isotopes (this study, colored symbols) with data from the literature (black and grey symbols) and ice core pCO_2 (LePetit at al., 2009; black line). Data from the two sites we examined reproduces the absolute values and amplitude of atmospheric pCO_2 as determined from ice cores, thereby validating our methodology.

Figure 3: Proxy data for the past 17 million years in the Western Equatorial Pacific compared to benthic oxygen isotope composites. **A.** Benthic $\delta^{18}O$ (blue line - Lisiecki and Raymo, 2005; black line – compilation from Zachos et al., 2008). **B.** Benthic $\delta^{13}C$ (black line – compilation from Zachos et al., 2008). C to E, colored is indicating the site (open grey=806, filled grey=807), symbols represent the species (circle=*T. sacculifer* and triangle=*G. ruber*).**C.** SST reconstructed at ODP Sites 806 and 807 using Mg/Ca ratios and equation S6 and S7 (this study). **D.** Seawater pH reconstructed from $\delta^{11}B$ of *T. sacculifer* and *G. ruber* using $\delta^{11}B_{seawater}$ from Greenop et al. (2017) (refer to text and supplement for calculations, this study). **E.** Reconstructed pCO_2 (µatm) using boron-based pH and alkalinity from Caves et al. (2016), data presented are from this study. Propagated uncertainties are given by eq. 18 for the dark (green or blue) envelope, while the light (green or blue) envelope are the uncertainties calculated based on eq. 17 (taking into account uncertainty on $\delta^{11}B_{seawater}$). Only data from this study are shown.

Figure 4: Proxy data from 17 to 6 million years, including the Middle Miocene Climate Transition (MMCT) and Micocene Climate Optimum (MCO), in the Western Equatorial Pacific compared to benthic oxygen isotope composites. **A.** Benthic $\delta^{18}O$ (black line – compilation from Zachos et al., 2008). **B.** Benthic $\delta^{13}C$ (black line – compilation from Zachos et al., 2008). C and D, colored is indicating the site (open grey=806, filled grey=807), symbols represent the species (circle=*T. sacculifer* and triangle=*G. ruber*).**C.** SST reconstructed at ODP Sites 806 and 807 using Mg/Ca ratios and equation S6 and S7 (this study). **D.** Reconstructed pCO_2 (µatm) using boron-based pH and alkalinity from Caves et al. (2016), data presented are from this study. Propagated uncertainties are given by eq. 18 for the dark (green or blue) envelope, while the light (green or blue) envelope are the uncertainties calculated based on eq. 17 (taking into account uncertainty on $\delta^{11}B_{seawater}$).

Figure 5: Proxy data from 7 to 1 million years, including the Warm Pliocene Transition (WPT), in the Western Equatorial Pacific compared to benthic oxygen isotope composites. **A.** Benthic $\delta^{18}O$ (black line – compilation from Zachos et al., 2008). **B.** Benthic $\delta^{13}C$ (black line – compilation from Zachos et al., 2008). C and D, colored is indicating the site (open grey=806, filled grey=807), symbols represent the species (circle=*T. sacculifer* and triangle=*G. ruber*).**C.** SST reconstructed at ODP Sites 806 and 807 using Mg/Ca ratios and equation S6 and S7 (this study). **D.** Reconstructed pCO_2 (µatm) using boron-based pH and alkalinity from Caves et al. (2016), data presented are from this study. Propagated uncertainties are given by eq. 18 for the dark (green or blue) envelope, while the light (green or blue) envelope are the uncertainties calculated based on eq. 17 (taking into account uncertainty on $\delta^{11}B_{seawater}$).

Figure 6: Proxy data from 1.5 to 0.5 million years, including the Middle Pleistocene Transition (MPT), in the Western Equatorial Pacific compared to benthic oxygen isotope composites. **A.** Benthic $\delta^{18}O$ (blue line – compilation from Lisiecki and Raymo, 2005). **B.** Benthic $\delta^{13}C$ (black line – compilation from Zachos et al., 2008). C and D, colored is indicating the site (open grey=806, filled grey=807), symbols represent the species (circle=*T. sacculifer* and triangle=*G. ruber*). **C.** SST reconstructed at ODP Sites 806 and 807 using Mg/Ca ratios and equation S6 and S7 (this study). **D.**

Reconstructed pCO_2 (µatm) using boron-based pH and alkalinity from Caves et al. (2016), data presented are from this study. Propagated uncertainties are given by eq. 18 for the dark (green or blue) envelope, while the light (green or blue) envelope are the uncertainties calculated based on eq. 17 (taking into account uncertainty on $\delta^{11}B_{seawater}$).

Figure 7: Proxy data from 1.5 to 0.5 million years, including the Middle Pleistocene Transition (MPT), in the Western Equatorial Pacific compared to benthic oxygen isotope composites. **A.** Benthic $\delta^{18}O$ (blue line – compilation from Lisiecki and Raymo, 2005, black line – compilation from Zachos et al. 2008). **B.** B. Records from Lithium isotopes ($\delta^{7}Li$, orange, Misra and Froelich, 2012) and Strontium isotopes ($^{87/86}Sr$, grey, Hodell et al., 1991, Farrel et al., 1995, Martin et al., 1999, Martin et al., 2004), both proxies for silicate weathering. Orange arrows represent the different weathering regimes as indicated by the $\delta^{7}Li$, black crosses are indication when changes in weathering regime occurs. **C.** Reconstructed pCO_2 (µatm) using boron-based pH and alkalinity from Caves et al. (2016), data presented are from this study. Propagated uncertainties are given by eq. 18 for the dark (green or blue) envelope, while the light (green or blue) envelope are the uncertainties calculated based on eq. 17 (taking into account uncertainty on $\delta^{11}B_{seawater}$). Colored is indicating the site (open grey=806, filled grey=807), symbols represent the species (circle=*T. sacculifer* and triangle=*G. ruber*). Rose band and dark rose band represent time of eruption of the Columbia river flood basalts (Hooper et al., 2002) and time of maximum eruption (Kasbohm and Schoene, 2018), respectively. Blue bands represent hypothesized La Madre intervals and red bands represent hypothesized El Padre intervals (Farell et al., 1995; Chaisson and Ravelo, 2000; Nathan and Leckie, 2009; Ford et al., 2012; Drury et al., 2018). The biogenic bloom in the EEP (Farell et al., 1995) and in the WEP (Berger et al., 1991), is hypothesized to have been driven by enhanced weathering that increased nutrient delivery to the global ocean (Hermoyian and Owen, 2001).

Table 1: Boxe core information.

Cruise	Leg	Hole	N (°)	E (°)	Depth (m)
ODP	130	807	3.61	156.62	3638
ODP	130	806	0.32	159.37	2521

Table 2: Analytical data and reconstructed parameters for ODP Sites 806 and 807.

Species	Sample	mcd	mbsf	Shell Wt	Age	δ¨B (1)	2SD$_{AE121}$	δ¨B (2)	2SD$_{AE121}$	δ¨B (average)	error	Mg/Ca	B/Ca	Li/Ca	Sr/Ca	SST	error	Salinity	TA	pH	error(1) up	error(1) down	error(2) up	error(2) down	pCO$_2$	error(1) up	error(1) down	error(2) up	error(2) down
				(µg)	(My)	(‰)	(‰)	(‰)	(‰)	(‰)	(‰)	(mmol/mol)	(µmol/mol)	(µmol/mol)	(mmol/mol)	(°C)	(°C)	(psu)	(µmol/kg)						(µatm)	(µatm)	(µatm)	(µatm)	(µatm)
G. ruber	806B 3 2 101-103	18.51	18.51	16.84	0.904	19.03	0.29			19.03	0.29	3.53	103	14.2	1.46	27.8	1.8	35.36	2246	8.20	0.08	0.08	0.03	0.02	221	61	48	19	18
G. ruber	806B 3 4 86-88	21.36	21.36	15.92	1.019	20.18	0.29			20.18	0.29	4.63	97	13.8	1.42	33.2	1.6	35.33	2243	8.28	0.07	0.07	0.03	0.02	165	43	35	14	14
G. ruber	806B 3 5 6-8	22.06	22.06	16.07	1.046	18.63	0.29			18.63	0.29	3.27	106	14.6	1.44	26.2	1.8	35.30	2241	8.16	0.09	0.08	0.03	0.02	249	72	55	22	21
G. ruber	806B 3 5 26-28	22.26	22.26	15.64	1.054	19.14	0.29			19.14	0.29	3.32	116	14.1	1.44	27.3	1.8	35.16	2241	8.22	0.08	0.07	0.03	0.02	209	57	45	18	17
G. ruber	806B 4 1 71-73	26.21	26.21	16.96	1.240	18.15	0.21			18.15	0.21	3.47	102	12.7	1.44	26.4	1.9	35.11	2230	8.091	0.09	0.08	0.03	0.02	308	93	69	23	22
G. ruber	806B 4 1 131-133	26.81	26.81	16.08	1.267	18.25	0.21			18.25	0.21	3.87	109	13.2	1.44	27.8	1.9	35.48	2228	8.09	0.09	0.08	0.03	0.02	308	92	69	23	22
G. ruber	806B 5 1 41-43	35.41	35.41	16.55	1.651	20.12	0.26			20.12	0.26	3.85	118	14.7	1.46	30.7	1.6	35.61	2206	8.29	0.07	0.07	0.03	0.02	158	41	33	13	12
G. ruber	806B 5 6 23-25	42.73	42.73	14.90	1.885	17.97	0.26			17.97	0.26	4.11	111	13.9	1.44	28.4	2.0	35.49	2192	8.03	0.10	0.09	0.03	0.02	354	113	83	30	29
G. ruber	806B 6 2 0-2	46.01	46.01	16.32	2.116	19.34	0.33			19.34	0.33	5.02	123	21.9	1.41	33.6	1.7	35.30	2183	8.16	0.08	0.07	0.03	0.02	231	64	51	22	21
G. ruber	806B 6 7 24-26	53.75	53.75	25.09	2.485	19.45	0.33	19.29	0.33	19.37	0.24	3.77	108	13.4	1.41	29.7	1.7	35.62	2173	8.21	0.08	0.07	0.03	0.02	205	55	44	16	15
G. ruber	806B 7 1 24-26	71.43	71.43	17.94	2.502	18.38	0.33	18.63	0.33	18.51	0.24	3.98	110	14.8	1.41	29.3	1.9	35.39	2172	8.10	0.09	0.08	0.03	0.02	288	84	64	23	22
G. ruber	806B 7 1 85-87	54.86	54.86	16.14	2.525	17.85	0.27			17.85	0.27	4.35	100	12.8	1.47	29.4	2.0	35.17	2172	8.00	0.10	0.09	0.03	0.03	386	127	92	35	33
G. ruber	806B 7 2 38-40	55.89	55.89	17.95	2.554	16.97	0.27			16.97	0.27	3.79	105	13.4	1.42	25.6	2.4	35.36	2171	7.89	0.13	0.11	0.04	0.03	534	219	143	55	50
G. ruber	806B 7 2 63-65	56.14	56.14	14.25	2.562	18.50	0.33			18.50	0.33	3.96	102	12.8	1.40	29.3	1.9	35.25	2171	8.10	0.09	0.08	0.04	0.03	289	87	66	29	27
G. ruber	806B 7 2 104-106	56.55	56.55	16.71	2.575	17.87	0.33	18.37	0.33	18.12	0.24	4.33	106	18.9	1.41	29.8	1.9	35.40	2170	8.04	0.10	0.08	0.03	0.02	346	107	80	28	27
G. ruber	806B 7 2 146-148	56.97	56.97	18.24	2.589	17.89	0.33			17.89	0.33	3.89	107	12.7	1.41	28.0	2.0	35.17	2170	8.02	0.10	0.09	0.04	0.03	363	120	88	39	35
G. ruber	806B 7 3 5-7	57.06	57.06	19.15	2.591	18.77	0.33	18.19	0.33	18.48	0.24	3.95	113	13.6	1.41	29.2	1.9	35.29	2170	8.10	0.09	0.08	0.03	0.02	291	86	65	23	22
G. ruber	806B 7 3 58-60	57.59	57.59	21.50	2.611	18.27	0.33			18.27	0.33	3.68	163	13.6	1.40	28.1	1.9	35.00	2169	8.08	0.10	0.09	0.04	0.03	307	95	72	31	29
G. ruber	806B 7 3 78-80	57.79	57.79	19.00	2.618	18.00	0.33			18.00	0.33	3.79	104	13.3	1.41	28.0	2.0	35.04	2169	8.04	0.10	0.09	0.04	0.03	345	111	82	36	33
G. ruber	806B 7 4 5-7	58.56	58.56	19.47	2.647	18.60	0.33	18.46	0.33	18.53	0.24	3.71	107	12.8	1.42	28.3	1.9	35.55	2168	8.11	0.09	0.08	0.03	0.02	278	81	62	22	21
G. ruber	806B 7 4 59-61	59.10	59.10	18.97	2.668	18.76	0.33	18.62	0.33	18.69	0.24	3.92	117	12.8	1.40	29.6	1.8	35.09	2168	8.12	0.09	0.08	0.03	0.02	269	77	59	21	20
G. ruber	806B 7 4 105-107	59.56	59.56	17.34	2.686	18.83	0.33	18.65	0.33	18.74	0.24	4.07	109	15.1	1.40	30.0	1.8	35.51	2167	8.12	0.09	0.08	0.03	0.02	267	76	59	21	20
G. ruber	806B 8 2 59-61	65.60	65.60	15.80	2.904	18.11	0.33	17.65	0.33	17.88	0.24	4.06	106	12.6	1.40	28.7	2.0	35.28	2161	8.01	0.10	0.09	0.03	0.02	373	121	88	31	29
G. ruber	806B 8 5 9-11	69.60	69.60	19.31	3.019	16.63	0.33	17.21	0.33	16.92	0.24	3.95	100	12.4	1.37	26.5	2.4	35.13	2158	7.87	0.13	0.11	0.04	0.03	559	232	150	52	48
G. ruber	806B 8 6 42-44	71.43	71.43	17.94	3.071	17.18	0.33			17.18	0.33	4.10	110	12.7	1.38	27.7	2.3	34.88	2157	7.90	0.12	0.11	0.05	0.04	505	197	134	60	53
T. sacculifer	806A 1 1 3-5	0.03	0.03	20.49	0.004	17.53	0.36			17.53	0.36	3.89	77	14.4	1.39	28.6	0.9	35.38	2266	8.15	0.09	0.08	0.03	0.03	244	71	55	25	23
T. sacculifer	806A 1 2 40-42	1.90	1.90	22.51	0.090	17.95	0.36			17.95	0.36	3.81	79	14.4	1.37	28.0	0.9	35.78	2264	8.18	0.08	0.08	0.03	0.03	222	63	50	22	21
T. sacculifer	806B 1 3 2-4	3.02	3.02	20.08	0.147	18.24	0.26	18.29	0.26	18.27	0.18	3.87	79	12.7	1.35	28.0	0.9	36.06	2261	8.22	0.08	0.07	0.02	0.02	335	106	79	36	33
T. sacculifer	806B 1 4 23-25	4.73	4.73	20.49	0.227	17.37	0.36	17.44	0.36	17.41	0.25	4.29	83	15.0	1.35	29.7	0.9	36.12	2249	8.12	0.08	0.08	0.02	0.02	196	52	41	13	13
T. sacculifer	806B 3 1 26-28	16.26	16.26	20.92	0.794	19.26	0.26			19.26	0.26	4.05	77	11.2	1.37	29.0	0.9	36.11	2249	8.28	0.07	0.07	0.02	0.02	264	76	58	21	20
T. sacculifer	806B 3 1 31-33	16.31	16.31	20.36	0.796	18.71	0.26			18.71	0.26	3.81	82	11.8	1.37	28.0	0.9	36.10	2248	8.25	0.08	0.07	0.02	0.02	161	42	34	13	12
T. sacculifer	806B 3 1 91-93	16.91	16.91	20.91	0.824	18.15	0.26			18.15	0.26	3.75	75	10.3	1.34	28.1	0.9	35.75	2247	8.19	0.08	0.08	0.02	0.02	181	48	38	14	14
T. sacculifer	806B 3 2 56-58	18.06	18.06	22.56	0.881	18.59	0.26			18.59	0.26	3.19	76	11.2	1.38	25.5	0.9	35.76	2245	8.25	0.08	0.07	0.02	0.02	213	59	46	17	16
T. sacculifer	806B 3 3 11-13	19.11	19.11	19.29	0.930	17.56	0.29			17.56	0.29	3.57	68	11.7	1.36	27.4	0.9	35.74	2244	8.16	0.08	0.08	0.03	0.03	180	48	38	14	14
T. sacculifer	806B 3 4 16-18	20.66	20.66	21.96	0.990	17.29	0.21			17.29	0.21	3.52	76	11.5	1.36	27.2	0.9	35.69	2244	8.11	0.09	0.08	0.02	0.02	240	69	53	21	20
T. sacculifer	806B 3 4 21-23	20.71	20.71	21.86	0.992	18.94	0.29			18.94	0.29	3.41	100	10.8	1.37	26.8	0.9	35.60	2241	8.27	0.08	0.07	0.02	0.02	273	80	60	20	19
T. sacculifer	806B 3 5 31-33	22.31	22.31	18.21	1.048	18.69	0.29			18.69	0.29	3.22	77	10.5	1.31	25.9	0.9	35.61	2230	8.28	0.08	0.07	0.02	0.02	168	45	36	14	14
T. sacculifer	806B 4 1 56-58	26.06	26.06	22.20	1.233	17.29	0.21			17.29	0.21	4.07	82	10.6	1.38	29.8	0.9	35.60	2228	8.08	0.09	0.08	0.02	0.02	164	44	35	14	13
T. sacculifer	806B 4 1 146-148	26.96	26.96	23.99	1.274	17.08	0.21			17.08	0.21	3.61	75	10.2	1.34	27.8	0.9	35.61	2219	8.07	0.09	0.08	0.02	0.02	295	87	66	22	21
T. sacculifer	806A 4 4 35-37	30.35	30.35	20.49	1.425	16.89	0.36			16.89	0.36	4.24	79	13.6	1.37	30.4	0.9	35.76	2263	8.04	0.09	0.09	0.03	0.03	306	93	69	23	22
T. sacculifer	806B 10 2 77-79	84.77	84.77	16.15	3.454	16.67	0.36	16.54	0.36	16.60	0.25	3.82	67	10.6	1.26	30.2	0.9	35.37	2147	8.04	0.09	0.08	0.02	0.02	323	100	75	27	26
T. sacculifer	806B 10 3 137-139	86.87	86.87	18.34	3.514	16.18	0.36	16.13	0.36	16.15	0.25	3.99	75	11.0	1.29	30.9	0.9	35.40	2146	7.97	0.10	0.09	0.03	0.03	398	133	96	35	33
T. sacculifer	806B 11 1 117-119	93.17	93.17	18.65	3.695	15.35	0.36			15.35	0.36	4.02	80	10.9	1.33	31.3	0.9	35.30	2141	7.86	0.12	0.11	0.04	0.04	531	209	143	67	59
T. sacculifer	806B 12 5 120-122	108.70	108.70	20.80	4.025	15.56	0.36			15.56	0.36	3.41	79	11.1	1.30	28.7	0.9	35.42	2133	7.90	0.12	0.10	0.04	0.04	475	183	126	59	52
T. sacculifer	806B 14 2 80-82	122.80	122.80	20.34	4.314	15.53	0.36			15.53	0.36	3.09	70	10.3	1.26	27.2	0.9	35.34	2125	7.92	0.12	0.10	0.04	0.04	451	174	120	56	50
T. sacculifer	806B 14 6 0-2	128.00	128.00	22.35	4.421	16.57	0.36	16.54	0.36	16.55	0.25	3.64	79	11.5	1.23	29.9	0.9	35.41	2122	8.00	0.10	0.09	0.03	0.03	360	118	86	31	30
T. sacculifer	806B 15 4 79-81	135.29	135.29	23.30	4.570	15.82	0.36			15.82	0.36	3.73	65	10.5	1.21	30.3	0.9	35.40	2118	7.90	0.12	0.10	0.04	0.04	476	180	125	59	52
T. sacculifer	806B 16 3 139-141	143.89	143.89	27.07	4.746	15.65	0.36			15.65	0.36	3.69	73	10.4	1.22	30.2	0.9	35.39	2114	7.85	0.13	0.11	0.04	0.04	550	226	151	72	63
T. sacculifer	806B 25 3 29-31	228.29	228.29	23.08	6.467	16.40	0.36			16.40	0.36	3.41	74	9.6	1.13	29.4	0.9	35.31	2028	8.02	0.10	0.09	0.03	0.03	323	106	79	37	33
T. sacculifer	806B 29 5 30-32	269.30	269.30	29.46	7.086	16.10	0.36	16.03	0.36	16.06	0.25	3.81	66	10.3	1.12	31.3	0.9	35.20	1989	7.93	0.11	0.09	0.03	0.03	406	142	100	37	35
T. sacculifer	806B 30 1 30-32	272.81	272.81	29.08	7.150	16.16	0.15			16.16	0.15	3.77	79	9.1	1.18	31.1	0.9	35.26	1984	7.95	0.10	0.09	0.02	0.02	384	130	92	27	26
T. sacculifer	806B 30 5 30-32	278.81	278.81	31.18	7.266	16.40	0.15	16.85	0.15	16.63	0.11	5.11	118	14.3	1.75	36.0	0.9	35.36	1975	7.94	0.10	0.09	0.02	0.02	391	126	91	24	24
T. sacculifer	806B 31 5 32-34	288.32	288.32	25.84	7.477	16.19	0.36	16.60	0.36	16.39	0.25	3.26	108	8.6	1.15	28.8	0.9	35.29	1958	8.04	0.10	0.09	0.03	0.02	297	94	70	26	25
T. sacculifer	806B 32 2 29-31	293.30	293.30	30.06	7.607	16.06	0.15	16.35	0.15	16.20	0.11	3.64	60	9.1	1.14	30.7	0.9	35.17	1947	7.97	0.10	0.09	0.02	0.02	358	119	84	23	22
T. sacculifer	806B 33 2 30-32	302.80	302.80	28.75	7.917	16.10	0.36			16.10	0.36	3.78	71	8.9	1.11	31.4	0.9	35.14	1922	7.97	0.10	0.09	0.04	0.03	352	121	88	41	38
T. sacculifer	806B 33 5 30-32	307.31	307.31	29.59	8.102	15.35	0.15			15.35	0.15	3.70	65	8.4	1.14	30.9	0.9	35.39	1916	7.88	0.11	0.10	0.02	0.02	448	167	113	32	32
T. sacculifer	806B 34 5 30-32	316.80	316.80	25.89	8.577	15.90	0.36			15.90	0.36	4.47	82	9.8	1.13	34.2	0.9	35.12	1916	7.96	0.10	0.09	0.04	0.03	361	122	90	42	38
T. sacculifer	806B 35X 5 30-32	320.30	320.30	24.79	8.772	14.67	0.36			14.67	0.36	4.06	75	10.1	1.19	32.5	0.9	35.38	1916	7.84	0.12	0.11	0.04	0.04	502	202	137	66	58
T. sacculifer	806B 36X 1 32-34	330.03	330.03	28.41	9.221	15.32	0.22			15.32	0.22	3.88	94	9.2	1.19	31.7	0.9	35.42	1912	7.92	0.11	0.09	0.02	0.02	404	143	100	35	33
T. sacculifer	806B 44X 5 34-36	413.54	413.54	25.80	12.208	14.93	0.36			14.93	0.36	4.70	73	12.1	1.13	35.4	0.9	35.17	1760	7.91	0.11	0.09	0.04	0.04	373	132	96	46	42
T. sacculifer	806B 46X 1 33-35	426.84	426.84	20.81	12.433	14.51	0.22			14.51	0.22	4.87	92	13.3	1.16	36.1	0.9	35.02	1733	7.89	0.10	0.09	0.02	0.02	385	134	95	35	33
T. sacculifer	806B 46X 5 33-35	432.84	432.84	32.85	12.547	14.97	0.22			14.97	0.22	4.46	121	13.0	1.20	34.5	0.9	35.33	1719	7.87	0.11	0.10	0.03	0.02	408	149	104	37	36
T. sacculifer	806B 47X 3 34-36	439.44	439.44	28.38	12.695	14.72	0.36			14.72	0.36	4.64	79	20.6	1.20	35.1	0.9	35.36	1701	7.87	0.11	0.10	0.04	0.04	404	151	107	52	47
T. sacculifer	806B 48X 2 34-36	447.64	447.64	29.59	12.930	16.40	0.29			16.40	0.29	4.54	92	15.2	1.30	35.1	0.9	34.92	1672	8.05	0.09	0.08	0.03	0.03	236	72	55	24	23
T. sacculifer	806B 48X 5 34-36	452.15	452.15	26.72	13.083	14.86	0.25			14.86	0.25	4.13	213	14.5	1.24	33.3	0.9	35.22	1658	7.92	0.10	0.09	0.03	0.03	342	120	86	34	32
T. sacculifer	806B 50X 2 32-34	*465.43*	*465.43*	*25.67*	13.540	13.85	0.36			13.85	0.36	4.49	75	11.9	1.25	35.0	0.9	34.91	1628	7.79	0.13	0.11	0.04	0.04	493	210	140	69	61
T. sacculifer	806B 51X 2 29-31	475.10	475.10	27.14	13.834	14.09	0.22			14.09	0.22	4.25	69	12.7	1.26	33.9	0.9	35.16	1609	7.82	0.12	0.10	0.03	0.03	444	178	119	44	41
T. sacculifer	806B 52X 2 31-33	484.41	484.41	28.48	14.087	14.54	0.26			14.54	0.26	4.94	68	11.0	1.18	36.6	0.9	34.91	1603	7.84	0.11	0.10	0.03	0.03	418	158	109	44	41
T. sacculifer	806B 52X 4 33-35	487.44	487.44	30.01	14.165	14.57	0.25			14.57	0.25	5.06	93	14.9	1.15	37.0	0.9	34.94	1608	7.83	0.11	0.10	0.03	0.03	434	166	114	45	43
T. sacculifer	806B 56X 2 35-37	523.15	523.15	26.90	15.670	13.52	0.29			13.52	0.29	4.76	65	10.9	1.13	36.3	0.9	34.75	1687	7.73	0.14	0.12	0.04	0.04	607	277	176	75	68
T. sacculifer	806B 58X 2 33-35	542.33	542.33	30.04	16.435	14.47	0.21			14.47	0.21	4.86	59	12.8	1.09	36.7	0.9	34.74	1687	7.83	0.11	0.10	0.03	0.02	458	174	119	42	40
T. sacculifer	807A 1 1 20-22	0.20	0.20	21.29	0.010	18.38	0.21	18.17	0.21	18.28	0.15	4.24	87	12.5	1.42	30.4	0.9	35.32	2266	8.20	0.08	0.07	0.02	0.02	212	57	44	13	13
T. sacculifer	807A 1 1 30-32	0.30	0.30	19.82	0.014	18.74	0.26			18.74	0.26	4.27	101	13.7	1.45	30.4	0.9	35.54	2266	8.24	0.07	0.07	0.02	0.02	181	48	38	14	14
T. sacculifer	807A 1 1 90-92	0.90	0.90	20.45	0.047	19.08	0.26			19.08	0.26	3.47	89	12.9	1.40	27.0	0.9	35.64	2266	8.31	0.07	0.07	0.02	0.02	152	40	32	12	11
T. sacculifer	807A 1 2 0-2	1.50	1.50	16.63	0.079	18.36	0.29			18.36	0.29	3.44	91	11.2	1.38	27.1	0.9	35.34	2266	8.27	0.08	0.07	0.02	0.02	173	46	37	15	14
T. sacculifer	807A 1 3 0-2	3.00	3.00	16.75	0.182	17.13	0.29			17.13	0.29	3.26	85	12.1	1.39	26.0	0.9	35.69	2265	8.17	0.09	0.08	0.03	0.03	237	68	53	21	20
T. sacculifer	807A 1 3 90-92	3.90	3.90	22.22	0.227	17.75	0.26	17.53	0.26	17.64	0.18	3.96	79	11.5	1.39	29.1	0.9	35.79	2265	8.14	0.08	0.08	0.02	0.02	249	70	54	17	16
T. sacculifer	807A 1 3 100-102	4.00	4.00	20.49	0.231	16.83	0.21			16.83	0.21	3.99	83	11.3	1.41	29.4	0.9	35.59	2264	8.07	0.09	0.08	0.02	0.02	309	92	69	22	22
T. sacculifer	807A 2 4 0-2	11.90	11.90	20.12	0.342	17.85	0.26			17.85	0.26	3.58	72	9.8	1.35	27.4	0.9	35.93	2259	8.19	0.08	0.08	0.02	0.02	218	61	47	17	17
T. sacculifer	807A 2 5 0-2	13.40	13.40	22.27	0.431	17.67	0.29			17.67	0.29	3.82	79	10.4	1.39	28.4	0.9	35.97	2257	8.14	0.08	0.08	0.03	0.03	248	71	55	22	21
T. sacculifer	807A 2 6 0-2	14.90	14.90	23.78	0.604	17.64	0.26			17.64	0.26	4.21	67	9.4	1.33	30.3	0.9	35.74	2253	8.11	0.09	0.08	0.02	0.02	276	80	61	22	21
T. sacculifer	807A 3 2 0-2	18.40	18.40	22.96	0.857	17.86	0.26			17.86	0.26	3.73	88	11.0	1.38	28.8	0.9	35.33	2247	8.15	0.08	0.08	0.02	0.02	245	70	54	20	19
T. sacculifer	807A 3 3 0-2	19.90	19.90	23.07	0.940	17.56	0.21	17.14	0.21	17.35	0.15	3.80	83	10.7	1.37	29.0	0.9	35.43	2245	8.09	0.09	0.08	0.02	0.02	288	84	63	18	17
T. sacculifer	807A 3 7 0-2	25.90	25.90	23.16	1.278	17.91	0.26			17.91	0.26	4.15	85	11.1	1.35	30.6	0.9	35.52	2228	8.13	0.08	0.08	0.02	0.02	256	73	56	21	20
T. sacculifer	807A 7 6 10-12	62.51	62.51	22.09	3.047	16.16	0.33			16.16	0.33	3.91	66	12.6	1.29	30.9	0.9	35.12	2158	7.94	0.11	0.10	0.04	0.03	435	154	110	49	44
T. sacculifer	807A 8 3 0-2	67.41	67.41	19.61	3.218	15.30	0.25			15.30	0.25	3.97	118	10.3	1.29	31.3	0.9	35.08	2153	7.85	0.12	0.10	0.03	0.03	561	222	148	54	49
T. sacculifer	807A 8 5 0-2	70.41	70.41	20.08	3.325	15.43	0.25			15.43	0.25	3.90	63	9.4	1.28	31.1	0.9	35.13	2150	7.86	0.12	0.10	0.03	0.03	535	207	139	50	47

T. sacculifer	807A 9 4 0-2	78.41	78.41	19.53	3.615	15.55	0.14		15.55	0.14	3.40	86	8.9	1.29	29.1	0.9	35.09	2143	7.91	0.11	0.10	0.02	0.02	472	173	117	31	30
T. sacculifer	807A 13 4 0-2	116.41	116.41	24.93	4.524	15.14	0.14		15.14	0.14	3.15	62	9.1	1.20	28.3	0.9	35.06	2120	7.82	0.13	0.11	0.02	0.02	599	259	162	41	40

mcd: meter composite depth
mbsf: meter below seafloor depth
Shell Wt: Average weight of individual shel
SST: Sea surface Temperature determined from Mg/Ca ratios, see text for calculations
error: propagated error with associated parameter
Salinity: see text for calculations
TA: Total Alkalinity from Caves et al., 2016
pH: pH calculated based on boron isotopes from this study, see text for calculations
pCO_2: Calcluated pCO_2 from pH and TA, see text for calculations
error (1): Propagated error for pH and pCO2 calculated from eq. S15 and eq. S17, respectively
error (2): Propagated error for pH and pCO_2 calculated from eq. S16 and eq. S18, respectively
up: propagated error above symbol
down: propagated error below symbol

Table 3: Comparison of reconstructed pCO_2 values for key intervals in the last 17 My.

Mid-Pleistocene transition (1.2-0.8 My)

MIS (G)	pCO_2 (µatm)	Reference	MIS (IG)	pCO_2 (µatm)	Reference	pCO_2 amplitude IG-G (µatm)
20	171	This study	**21**	245	This study	74
22	180	This study	**23**	222	This study	42
24	*nd*		**25**	288	This study	*nd*
26	168	This study	**27**	*nd*		*nd*
28	165	This study	**29**	*nd*		*nd*
30	164	This study	**31**	295	Hönisch et al., 2009 (N-TIMS)	131
32	218	Chalk et al., 2017	**33**	323	Chalk et al., 2017	105
34	197	Chalk et al., 2017	**35**	315	Chalk et al., 2017	118
36	189	Chalk et al., 2017	**37**	295	This study, Chalk et al., 2017	106
			39	306	This study	*nd*

Early Pliocene Warm Period (4.7-4.5 My)

pCO_2 (µatm)	Reference
541 ± 124	This study (2 SD, n=3)

Middle Pliocene Warm Period (3.29-2.97 My)

pCO_2 (µatm)	Reference
515 ± 119	This study (2 SD, n=4)
320 ± 130	Martinez-Boti, 2015b (2 SD, n=8)

Miocene Climate Optimum (17-14 My)

pCO_2 (µatm)	Reference
479 ± 173	This study (2 SD, n=4)
350-400	Foster et al., 2012
300-500	Greenop et al., 2014
470-630	Sosdian et al., 2018

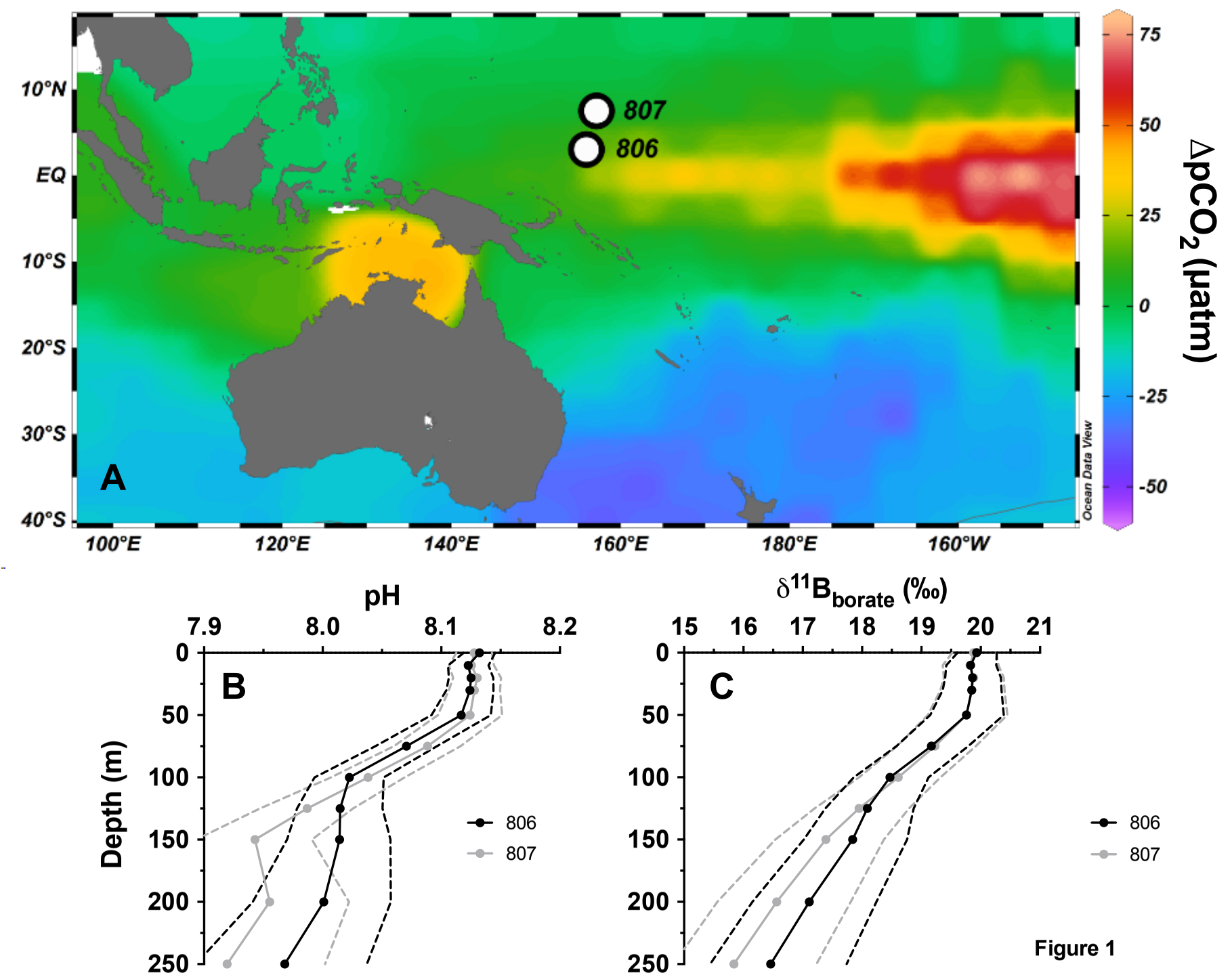
A
807
806
10°N
EQ
10°S
20°S
30°S
40°S
100°E
120°E
140°E
160°E
180°E
160°W
75
50
25
0
-25
-50
ΔpCO2 (µatm)
Ocean Data View
B
pH
7.9
8.0
8.1
8.2
Depth (m)
0
50
100
150
200
250
806
807
C
δ11Bborate (‰)
15
16
17
18
19
20
21
806
807

Figure 1

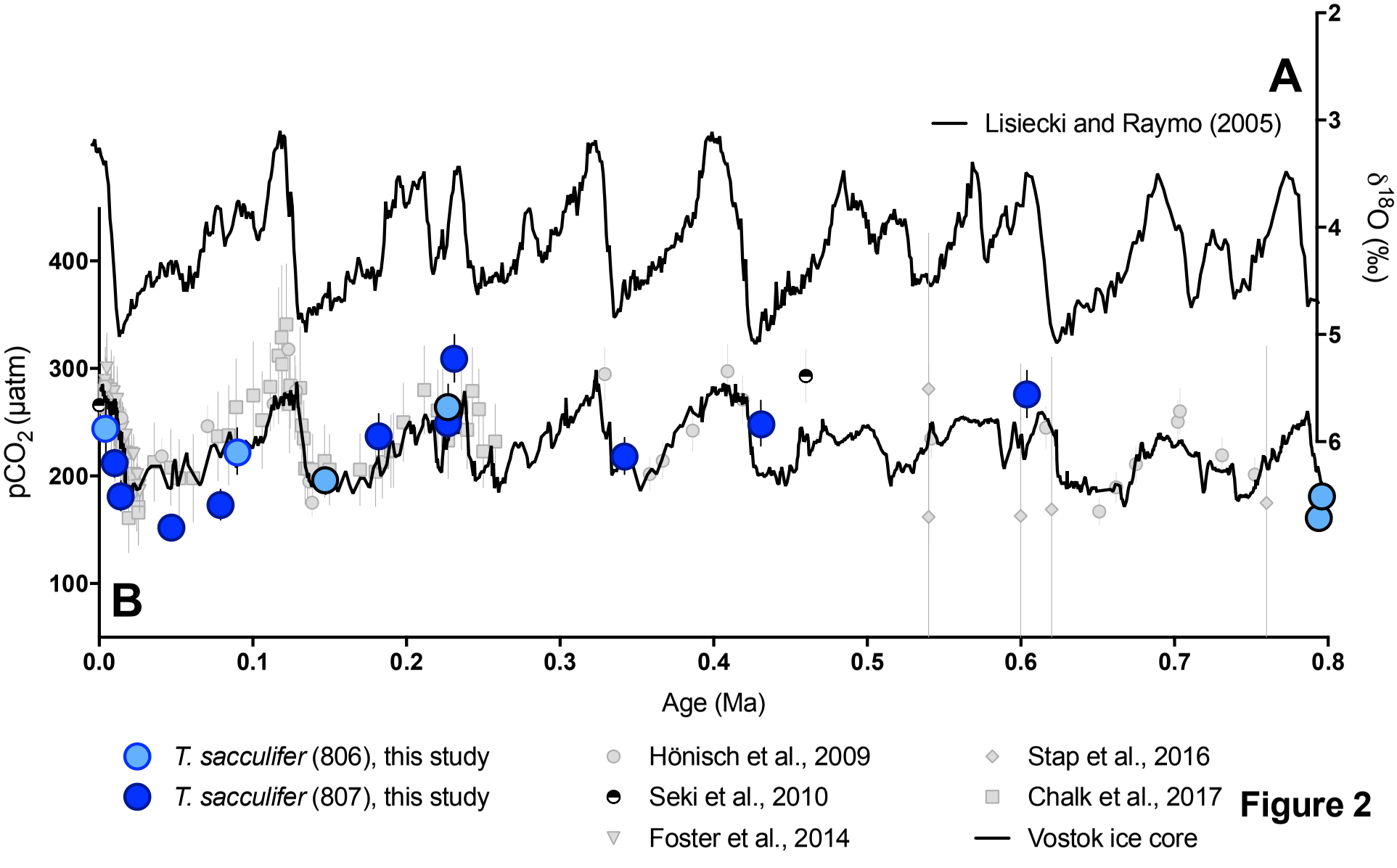
A
Lisiecki and Raymo (2005)
$\delta^{18}O$ (‰)
2
3
4
5
6
pCO_2 (µatm)
400
300
200
100
B
0.0
0.1
0.2
0.3
0.4
0.5
0.6
0.7
0.8
Age (Ma)
T. sacculifer (806), this study
T. sacculifer (807), this study
Hönisch et al., 2009
Seki et al., 2010
Foster et al., 2014
Stap et al., 2016
Chalk et al., 2017
Vostok ice core

Figure 2

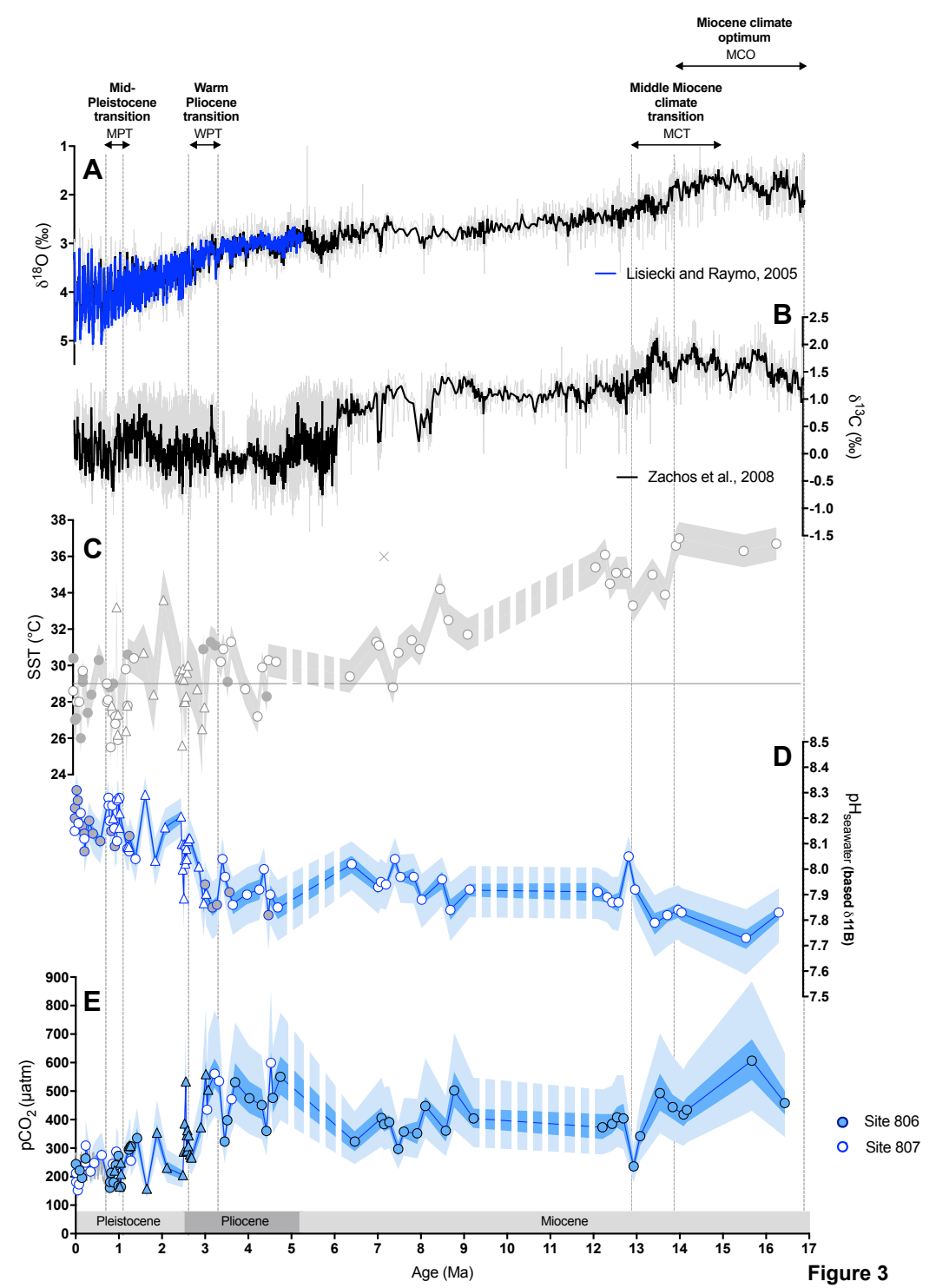
Miocene climate optimum
MCO
Mid-Pleistocene transition
MPT
Warm Pliocene transition
WPT
Middle Miocene climate transition
MCT
A
B
C
D
E
δ18O (‰)
Lisiecki and Raymo, 2005
δ13C (‰)
Zachos et al., 2008
SST (°C)
pHseawater (based δ11B)
pCO2 (µatm)
Site 806
Site 807
Pleistocene
Pliocene
Miocene
Age (Ma)

Figure 3

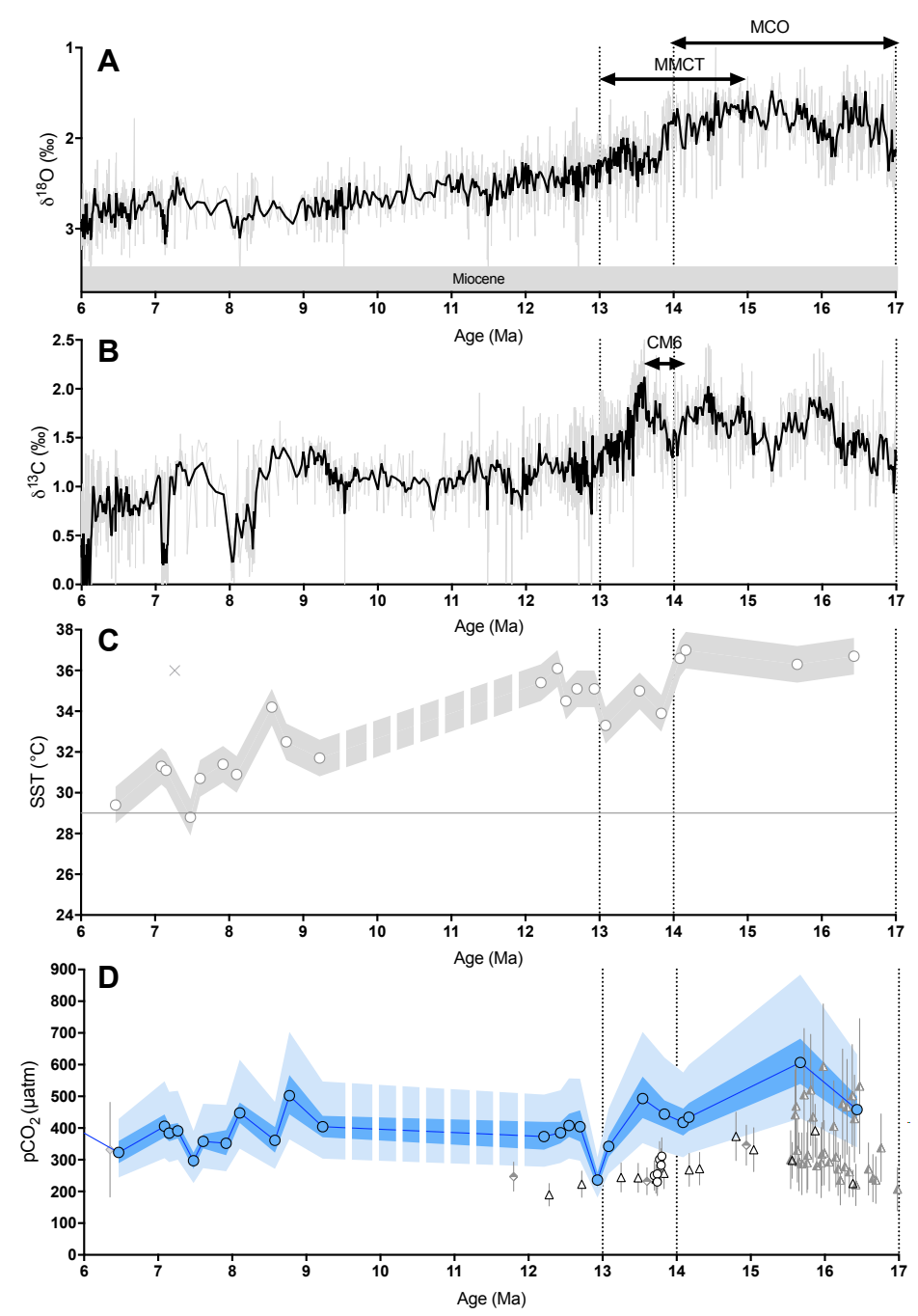
A
MCO
MMCT
Miocene
δ18O (‰)
Age (Ma)
B
CM6
δ13C (‰)
Age (Ma)
C
SST (°C)
Age (Ma)
D
pCO2 (µatm)
Age (Ma)
Site 806
Stap et al., 2016 (1264)
Greenop et al., 2014 (761B)
Foster et al., 2012 (761B)
Foster et al., 2012 (962A)
Badger et al., 2013

Figure 4

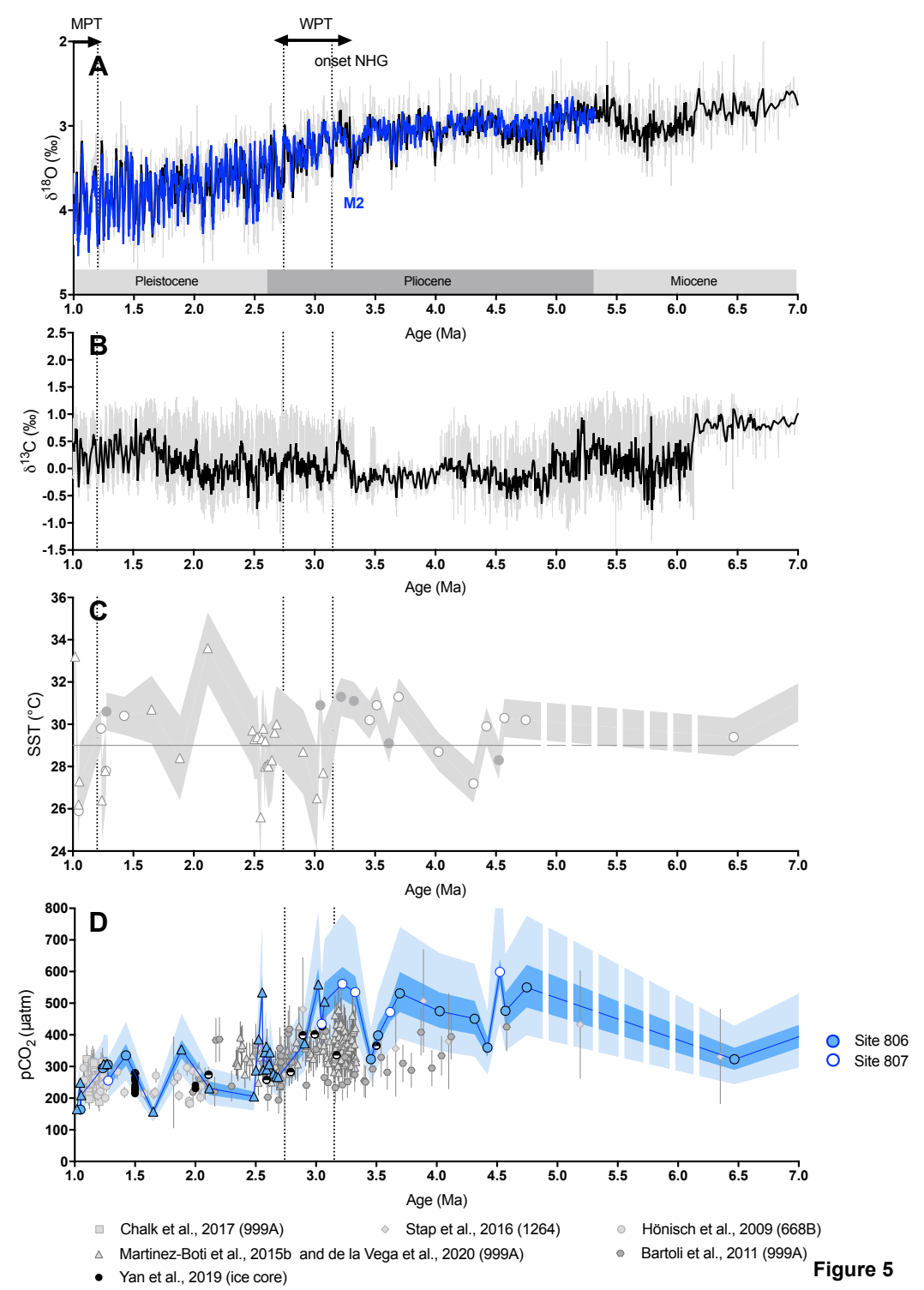
MPT
WPT
onset NHG
A
M2
δ18O (‰)
Pleistocene
Pliocene
Miocene
Age (Ma)
B
δ13C (‰)
Age (Ma)
C
SST (°C)
Age (Ma)
D
pCO2 (µatm)
Age (Ma)
Site 806
Site 807
Chalk et al., 2017 (999A)
Stap et al., 2016 (1264)
Hönisch et al., 2009 (668B)
Martinez-Boti et al., 2015b and de la Vega et al., 2020 (999A)
Bartoli et al., 2011 (999A)
Yan et al., 2019 (ice core)

Figure 5

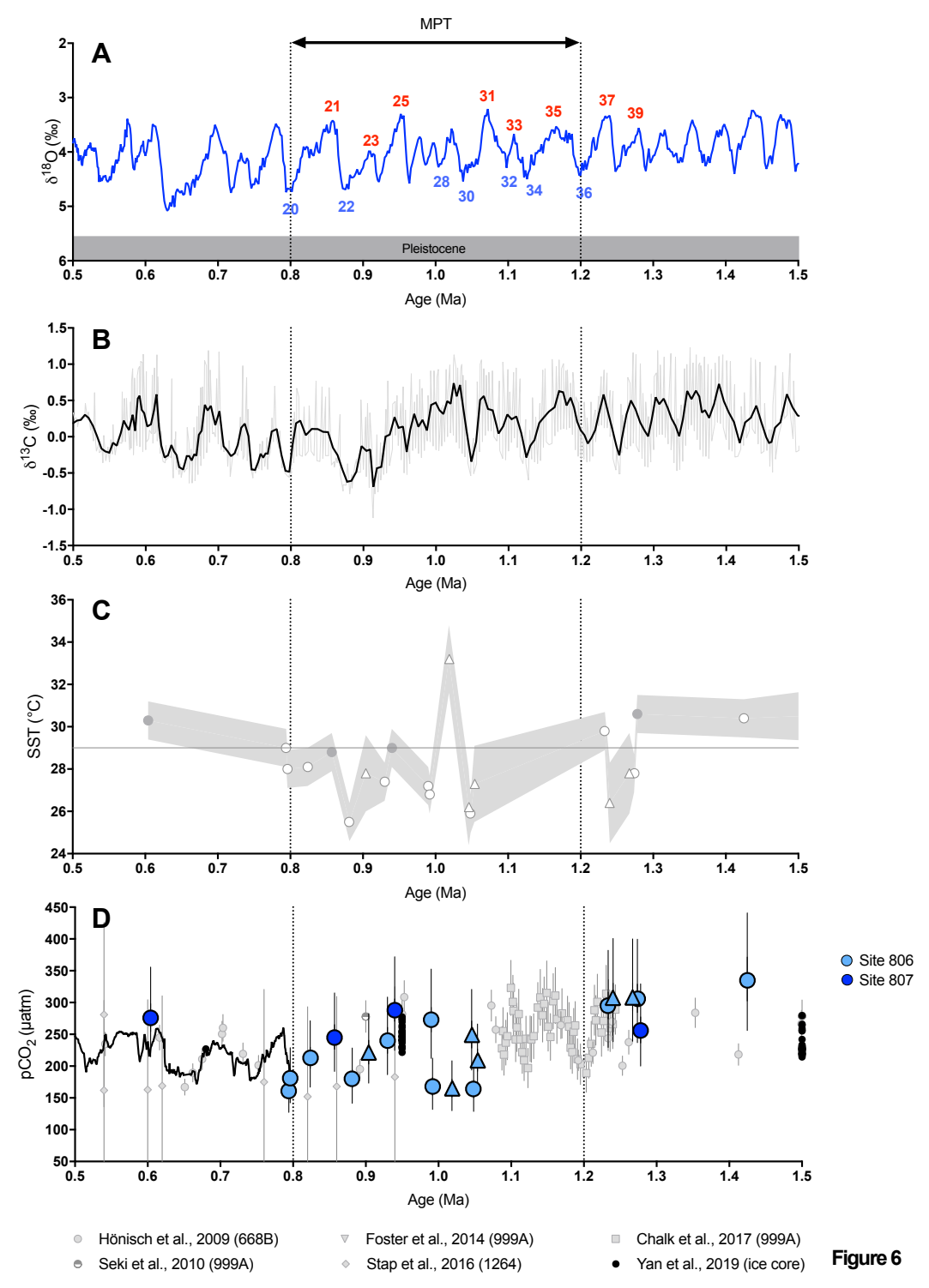
A
MPT
δ18O (‰)
Pleistocene
Age (Ma)
B
δ13C (‰)
Age (Ma)
C
SST (°C)
Age (Ma)
D
pCO2 (µatm)
Age (Ma)
Site 806
Site 807
Hönisch et al., 2009 (668B)
Seki et al., 2010 (999A)
Foster et al., 2014 (999A)
Stap et al., 2016 (1264)
Chalk et al., 2017 (999A)
Yan et al., 2019 (ice core)

Figure 6

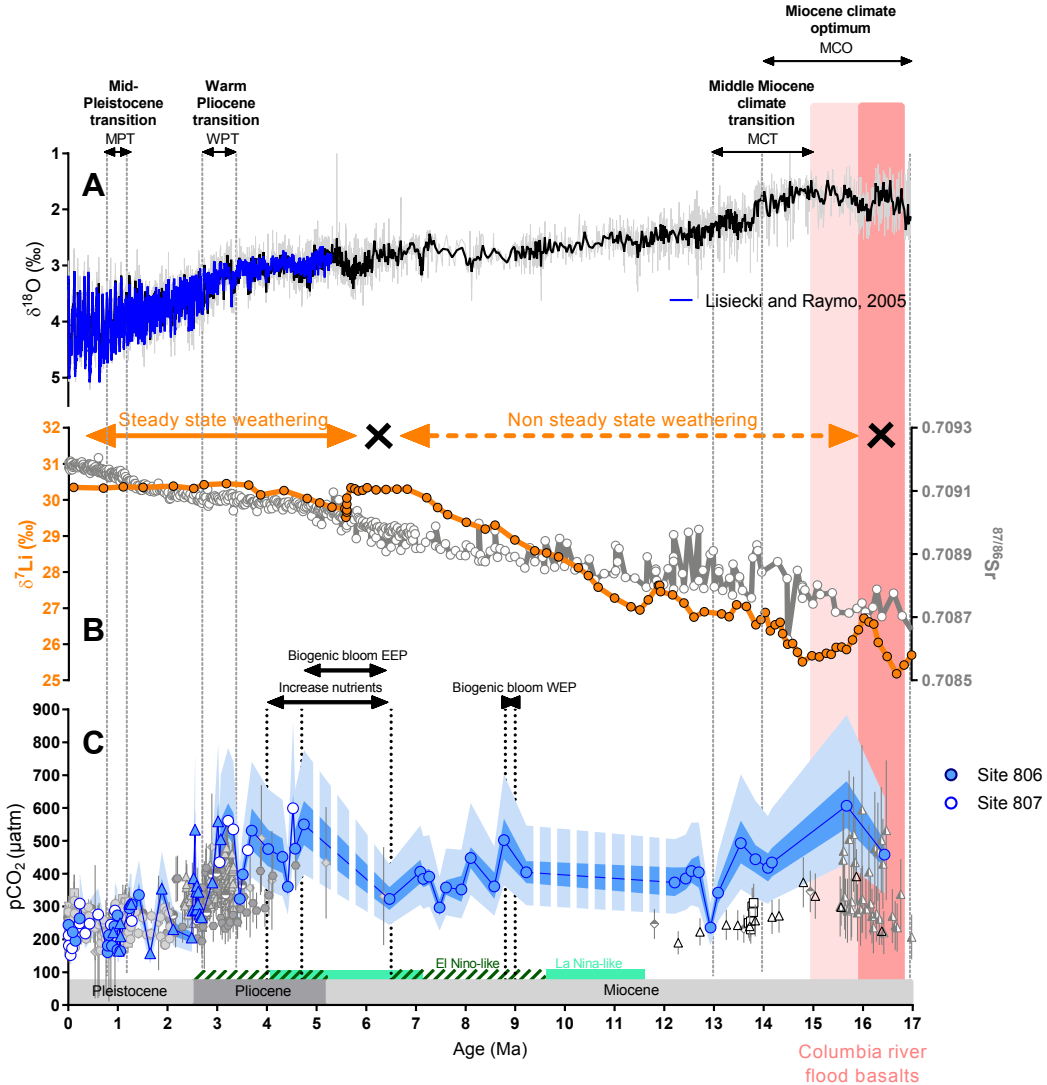

- Chalk et al., 2017 (999A)
- Stap et al., 2016 (1264)
- de La Vega 2020 Martinez Boti., 2015b (999)
- Foster et al., 2014 (999A)
- Greenop et al., 2014 (761B)
- Badger et al., 2013
- Foster et al., 2012 (962A)
- Foster et al., 2012 (761B)
- Bartoli et al., 2011 (999A)
- Seki et al., 2010 (999A)
- Hönisch et al., 2009 (668B)

Figure 7

SUPLEMENTAL INFORMATIONS

Atmospheric CO_2 reconstruction for the last 17 Ma based on foraminiferal $\delta^{11}B$ measurements for Ocean Drilling Program Sites 806 and 807 in the Western Equatorial Pacific warm pool

Maxence Guillermic[1,2], Sambuddha Misra[3,4], Robert Eagle[1,2], Aradhna Tripati [1,2]

[1]Department of Atmospheric and Oceanic Sciences, Department of Earth, Planetary, and Space Sciences, Center for Diverse Leadership in Science, Institute of the Environment and Sustainability, University of California – Los Angeles, Los Angeles, CA 90095 USA

[2]Laboratoire Géosciences Océan UMR6538, UBO, Institut Universitaire Européen de la Mer, Rue Dumont d'Urville, 29280, Plouzané, France

[3]The Godwin Laboratory for Palaeoclimate Research, Department of Earth Sciences, University of Cambridge, UK

[4]Indian Institute of Science, Centre for Earth Sciences, Bengaluru, Karnataka 560012, India

Supplemental Methods

1.1 Potential contamination

We found no evidence for contamination of TE (including Mg/Ca) arising from the presence of silicate minerals or Mn-Fe-Oxide coatings. Contamination of samples by silicate minerals was monitored using Fe/Mg ratios. Samples with Fe/Mg > 0.1 mol/mol are typically rejected due to potential contamination by silicate minerals (Barker et al., 2003). Our samples have an average Fe/Mg of 0.034 ± 0.07 mol/mol (2 SD, n=106), indicating that silicate minerals have been efficiently removed during our cleaning. Contamination by clays was monitored using Ti/Ca no correlations were found between Ti/Ca and Mg/Ca (R^2=0.0066) or with B/Ca (R^2=0.0237). Contamination by Mn-Fe oxides is detected using Mn/Ca ratios and Fe/Ca ratios. Our samples have Mn/Ca ratios of 0.12 ± 0.11 mmol/mol (2 SD, n=108) consistent with previous published data of cleaned samples (Wara et al., 2005). No correlations was observed between Mg/Ca and Fe/Ca (R^2=0.0841) or between Mg/Ca and Mn/Ca (R^2=0.0161). No significant correlation was observed between B/Ca and Mn/Ca (R^2=0.0011) or B/Ca and Fe/Ca (R^2=0.0132) ratios.

2.7 Calculations of temperature, salinity, pH, and pCO_2

Analyses of $\delta^{11}B$, $\delta^{18}O$ and elemental ratios (eg., Mg/Ca, B/Ca) were used to reconstruct the chemical and physical properties of seawater over the last 17 My of the Western Equatorial Pacific (Fig. S1).

2.7.1 Salinity reconstruction

Salinity was reconstructed using the relative sea level (RSL) reconstruction from Stap et al. (2017) and equation 2:

$$S=S_{modern}/3800*(3800+RSL) \qquad \textbf{eq. 2}$$

S_{modern} is the modern salinity corresponding to the depth habitat of the foraminifera at the site of interest. The depths used were 125 m for *T. sacculifer* and 80m for *G. ruber* (Rickaby et al., 2005; Guillermic et al., 2020). At Site 806, values for S_{modern} of 35.38 was used for *T. sacculifer* and 35.01 was used for *G. ruber*. At Site 807, a value of 35.05 was used for *T. sacculifer*.

2.7.2. Temperature

Paleotemperatures were calculated using Mg/Ca ratios of planktic foraminifera. A number of factors have been shown to impact Mg/Ca ratios and calculated paleotemperature. Factors identified in prior studies include salinity and pH effects on Mg/Ca, seawater Mg/Ca ratios, cleaning methodology, dissolution, and basin-specific equations, as discussed in more detail below. Below we describe some of the prior work that was factored into the regional mono-specific equations we used for calculating temperature from Mg/Ca.

2.7.2.1 Prior work showing evidence for salinity and pH effects on Mg/Ca-T

Studies have found that Mg/Ca ratios in foraminifera are impacted by salinity (Nürnberg et al., 1996; Hönisch et al., 2013) and pH or [CO_3^{2-}] (Russell et al., 2004; Kisakürek et al., 2008; Evans et al., 2016; Gray et al., 2018; Gray and Evans, 2019). Based on culture experiments, Gray and Evans (2019) reported impacts of both salinity and pH on *G. ruber* but only a salinity effect on *T. sacculifer*, and derived the following equations:

$$\text{SST}\ (T.sacculifer) = (Ln(\frac{Mg}{Ca}test) - 0.054 * (S - 35) + 0.24)/0.062 \quad \textbf{eq. 3}$$

$$SST\ (G.ruber) = (Ln(\frac{Mg}{Ca}test - 0.036 * (S - 35) + 0.87 * (\text{pH} - 8) + 0.03)/0.064 \quad \textbf{eq. 4}$$

2.7.2.2 Prior work showing evidence for variations in Mg/Ca ratios of seawater

Over timescales of 10^6-10^7 years, Mg/Ca_{sw} can vary. Evidence from evaporites, carbonate veins, fossil corals and models suggests that seawater Mg/Ca_{sw} ratios have varied through time with variations of ~3 mol/mol (Horita et al., 2002; DeFantle and Paolo, 2006; Coggon et al., 2011; Brennan et al., 2013; Gothman et al., 2015). These studies do not agree on the timing of changes in Mg/Ca_{sw}. Gothman et al. (2015) made measurements of corals and also compiled different seawater archives including carbonate veins, gastropods, brachiopods, fish teeth, and found that values of Mg/Ca_{sw} of 2.5 mol/mol occurred ~25 My. To correct for secular variations in Mg/Ca_{sw} we used the approach of O'Brien et al. (2014), theoretical work from Evans and Muller, (2012), and the Mg/Ca_{sw} record of Gothman et al. (2015). The equations we utilized are adapted from Dekens et al. (2002):

$$\text{SST}\ (T.sacculifer) = (Ln(\frac{Mg}{Ca}test * \frac{Mg^H}{Ca}sw_{t0}) \quad - Ln(0.37 * \frac{Mg^H}{Ca}sw_t))/0.09 + 0.36 * C + D \quad \textbf{eq. 5}$$

$$\mathrm{SST}\ (G.ruber) = (Ln(\frac{Mg}{Ca}test * \frac{Mg^H}{Ca}sw_{t0}) \quad - Ln(0.37 * \frac{Mg^H}{Ca}sw_t))/0.09 + 0.61 * C + D$$

eq. 6

Specifically H refers to the power components of the power law relationship between the Mg partition coefficient and Mg/Ca_{sw}, with a value of 0.41 for *T. sacculifer* (Delaney et al., 1985) which we also assume is the same for *G. ruber*. C is the depth of the site. D refer to a basin-specific offset, which is 2 °C for *T. sacculifer* and 2.9 °C for *G. ruber* for the Pacific Ocean, (Table S1).

2.7.2.3 Prior work on reductive cleaning effects on Mg/Ca

The use of a reductive step in cleaning has been shown to lower Mg/Ca_{test} ratios in planktic (Barker et al., 2003; Bian et al., 2010; Johnstone et al., 2016) and benthic foraminifera (Yu et al., 2007a), and contribute to offsets between studies using different methodologies. A decrease in Mg/Ca_{test} of 6-9% was reported for *T. sacculifer* by Bian et al. (2010), and of 5% by Johnstone et al. (2016). A decrease of 4% was reported for *G. ruber* by Johnstone et al. (2016).

2.7.2.4 Mg/Ca-SST equations used for this study

Based on the above equations from Gray and Evans (2019) (eq. 3 and 4), we incorporated a term to account for changes in the Mg/Ca ratio of seawater, and based on results from Dekens et al., (2002) we incorporated two terms to account for dissolution (C) and basin-specific offsets (D), and used an iterative approach for our calculations to account for pH effect on *G. ruber (*Gray and Evans, 2019). The equations we used are:

$$\mathrm{SST}\ (T.sacculifer) = \frac{Ln\left((\frac{Mg}{Ca}test * 1.05 * \frac{\frac{Mg^H}{Ca}sw_{t0}}{\frac{Mg^H}{Ca}sw_t}\right) - 0.054 * (S-35) + 0.24}{0.062} + 0.36 * C + 2.0 \qquad \textbf{eq. 7}$$

$$\mathrm{SST}\ (G.ruber) = \frac{Ln\left(\frac{Mg}{Ca}test * 1.05 * \frac{\frac{Mg^H}{Ca}sw_{t0}}{\frac{Mg^H}{Ca}sw_t}\right) - 0.036 * (S-35) + 0.87 * (\mathrm{pH}-8) + 0.03}{0.064} + 0.61 * C + 2.9$$

eq. 8

With H being the power components of the power relationship between the Mg partition coefficient and Mg/Ca_{sw}, 0.41 for *T. sacculifer* (Delaney et al., 1985). We use the same value for *G. ruber*. C is the depth of the core (km). In order to take the impact of reductive cleaning into account we applied a decrease of 5% for *G. ruber* and *T. sacculifer* (Bian et al., 2010 and Johnstone et al., 2016).

Given evidence for a pH effect on Mg/Ca-SST calibration for *G. ruber*, we used an iterative approach for our calculations, following Gray and Evans, (2019). Up to 4 iterations were needed to achieve a difference in SST with the previous iteration of <0.05°C and a difference in pH of <0.001. For this iterative approach, we first calculate pH_1 from foraminiferal $\delta^{11}B$, then calculate SST_1 from pH_1, then calculate pH_2 with SST_1, and then repeat.

2.8 $\delta^{11}B_{borate}$ from $\delta^{11}B_{carbonate}$

The use of $\delta^{11}B$ in foraminiferal carbonate to calculate seawater $\delta^{11}B_{borate}$, and derived pH and pCO_2 values**,** has been shown to accurately replicate pCO_2 records independently determined from ice cores and using oceanographic data, if several factors are taken into account (Chalk et al., 2017; Guillermic et al., 2020). These factors include mono-specific calibrations, size fraction or shell weight, basin, and water depth. In order to accurately reconstruct seawater pH (and pCO_2) from $\delta^{11}B$ of foraminifera, mono-specific calibrations are needed to convert $\delta^{11}B_{carbonate}$ to $\delta^{11}B_{borate}$. Recent culture and field-based calibrations have refined the sensitivities of $\delta^{11}B_{carbonate}$ to $\delta^{11}B_{borate}$ for different foraminiferal species (Henehan et al., 2016; Raitzsch et al., 2018; Guillermic et al., 2020). For *T. sacculifer* and *G. ruber,* the sensitivities of $\delta^{11}B_{carbonate}$ to $\delta^{11}B_{borate}$ are 0.82 and 0.58, respectively (Raitzsch et al., 2018; Guillermic et al., 2020). As with Mg/Ca, the intercepts are prone to large uncertainties and are commonly adjusted based on core-top data, in order to yield the expected pre-industrial pH or pCO_2 value at the site being examined (Chalk et al., 2017; Sosdian et al., 2018). The rationale for this correction is the impact of the depth habitat on microenvironment pH and subsequent $\delta^{11}B_{carbonate}$ (Hönisch and Hemming, 2004; Guillermic et al., 2020) and/or preferential dissolution of gametogenic calcite (Ni et al., 2007). It is also possible that these offsets may reflect observed size effects on *G. ruber* as well as *T. sacculifer* (Henehan et al., 2013; Hönisch et al., 2019). For *T. sacculifer*, a relationship between shell size and $\delta^{11}B_{carbonate}$ has been observed in the WEP (Hönisch and Hemming, 2004; Ni et al., 2007). Hönisch and Hemming, (2004) also reported that values for the 515-865 μm size fraction yielded values of 21.76 ‰,

and determined a size-fraction specific relationship. Here, we modify this approach to develop a shell-weight specific relationship:

$$\text{Size offset (‰)} = 21.76 - (0.06522 * \text{Weight/shell (µg)} + 17.38) \quad \textbf{eq. 9}$$

We adapted the equation for *T. sacculifer* from Guillermic et al. (2020):

$$\delta^{11}B_{borate} = [(\delta^{11}B_{T.\ sacculifer} + \text{Size offset}) - 4.09\ (\pm 0.86)] / 0.83\ (\pm 0.48) \quad \textbf{eq. 10}$$

Due to the lack of coretop measurements for *G. ruber* from this study, we selected three control points at Marine isotope stages (MIS) 30, 37 and 39 (Lisiecky and Raymo, 2005) times when both *T. sacculifer* and *G. ruber* where measured to determine appropriate offsets for both Mg/Ca and $\delta^{11}B$ that yield (Table S1 and S2) the best agreement between the species. This was used to adapt the equation from Guillermic et al. (2020) for *G. ruber*:

$$\delta^{11}B_{borate} = [(\delta^{11}B_{G.\ ruber} + 2.0) - 9.11\ (\pm 0.73)] / 0.58\ (\pm 0.91) \quad \textbf{eq. 11}$$

2.9 Constants

Temperature, salinity and pressure were used to calculate the different dissociation constants and parameters. We used K_1, K_2 from Lueker et al. (2000), K_B from Dickson, (1990), KSO_4 from Dickson, (1990), KF from Peres and Fraga, (1987) and total boron from Lee et al. (2010).

2.10 pH calculations

The quantitative estimation of pH using downcore $\delta^{11}B_{carbonate}$ requires: 1) calculations of the borate isotopic composition of seawater ($\delta^{11}B_{borate}$), 2) constraints on the secular variation of the boron isotopic composition of seawater ($\delta^{11}B_{seawater}$), 3) the fractionation factor (α) between $B(OH)_3$ and $B(OH)_4^-$ and 4) the calculations of acid/base equilibrium constants based temperature, salinity and pressure. To translate our $\delta^{11}B$ measurements to pH, we used the following relationship (Hemming and Hanson, 1992):

$$pH = pK_B^* - \log\left(\frac{\delta^{11}B_{seawater} - \delta^{11}B_{borate}}{\delta^{11}B_{seawater} - \alpha * \delta^{11}B_{borate} - \varepsilon}\right) \quad \textbf{eq. 12}$$

pK_B^* is the dissociation constant between the two boron species (8.5975 at 25 °C and a salinity of 35 psu, Dickson, 1990). A fractionation between $B(OH)_3$ and $B(OH)_4^-$ (ε) of 27.2 ± 0.6 ‰

was empirically determined by Klochko et al. (2006) in seawater and confirmed independently using a different method by Nir et al. (2015).

A few studies have attempted to reconstruct secular variations of $\delta^{11}B_{seawater}$ (Lemarchand et al., 2000; Foster et al., 2012; Raitzsch and Hönisch, 2013; Greenop et al., 2017). For our work, we first compared different scenarios (Fig. S1A). These scenarios are modeled values of $\delta^{11}B_{seawater}$ based on constraints on the boron budget from Lemarchand et al. (2000) (labeled as scenario L02), a second modeled history that assumed changes in seawater pH from Raitzsch and Hönisch (2013) (labeled as scenario R&H13), and a third scenario that also considered constraints on pH gradients from $\delta^{13}C$ measurements published by Greenop et al. (2017) (labeled as scenario G17).

2.11 pCO_2 calculations

The carbonate system has two degrees of freedom, meaning that if two parameters of the carbonate system are known all the others can be calculated. For this study, we utilized pH calculated using $\delta^{11}B_{borate}$, and total alkalinity (TA) as a second parameter that are shown in Fig. S2A. We used three different alkalinity scenarios for our calculations (Tyrell and Zeebe, (2004) (T&Z-04), Ridgwell and Zeebe, (2005) (R-05) and Caves et al. (2016) (Caves-16)). For all calculations, we used CO_2sys from Pierrot et al. (2006).

2.12 Error propagation for temperature (T), pH and pCO_2

The main source of uncertainty in reconstructed pCO_2 comes from the errors in pH. Table S3 summarizes the sensitivity of pH and pCO_2 to different variables. The individual uncertainties were propagated in quadrature to combined uncertainties for temperature (δT), pH (δpH) and pCO_2 (δpCO_2) (eq. 13, 14, 15, 16 and 17). Minimum and maximum propagated uncertainties were derived separately for pH and pCO_2. δpCO_2 (A) is the full uncertainty propagation, δpCO_2 (B) is the uncertainty propagation without taking into account the $\delta^{11}B_{sw}$. Both are shown in the figures and discussed below.

$$\delta T_{G.\ ruber} = \sqrt{(\delta T\_Mg/Ca)^2 + (\delta T\_Salinity)^2 + (\delta T\_pH)^2} \quad \textbf{eq. 13}$$

$$\delta T_{T.\ sacculifer} = \sqrt{(\delta T\_Mg/Ca)^2 + (\delta T\_Salinity)^2} \quad \textbf{eq. 14}$$

$$\delta pH\ (A) = \sqrt{(\delta pH\_Temperature)^2 + (\delta pH\_Salinity)^2 + (\delta pH\_\delta^{11}B_{sw})^2 + (\delta pH\_\delta^{11}B_{carbonate})^2}$$

eq.15

$$\delta pH\ (B) = \sqrt{(\delta pH\_Temperature)^2 + (\delta pH\_Salinity)^2 + (\delta pH\_\delta^{11}B_{carbonate})^2} \quad \textbf{eq.16}$$

$$\delta pCO_2\,(A) = \sqrt{\begin{array}{c}(\delta pCO_2\_Temperature)^2 + (\delta pCO_2\_Salinity)^2 + (\delta pCO_2\_\delta^{11}B_{sw})^2 + \\ (\delta pCO_2\_\delta^{11}B_{carbonate})^2 + (\delta pCO_2\_Alkalinity)^2\end{array}} \quad \textbf{eq. 17}$$

$$\delta pCO_2\,(B) = \sqrt{\begin{array}{l}(\delta pCO_2\_Temperature)^2 + (\delta pCO_2\_Salinity)^2 + \\ (\delta pCO_2\_\delta^{11}B_{carbonate})^2 + (\delta pCO_2\_Alkalinity)^2\end{array}} \quad \textbf{eq. 18}$$

With for example, "δpCO_2_Temperature" being the uncertainty in pCO_2 due to temperature.

Tables and Figures

Table S1: Control points for a 2‰ offset used for G. ruber.

Table S2: Comparaison of the control points reconstructions between T. sacculifer and G. ruber for MIS 30, 37 and 39, using different offsets (see text).

Table S3: Sensitivity tests for reconstructed pH and pCO2 (G17, Caves-16), all results are given as the minimum and maximum variation (%) observed in our data.

Figure S1: Results for the past 17 million years. A. Benthic $\delta^{18}O$ (blue line - Lisiecki and Raymo, 2005; black line – compilation from Zachos et al., 2008). B. $\delta^{11}B$ of *T. sacculifer* and *G. rube*r at sites 806, 807. C. B/Ca ratios. D. Mg/Ca ratios. E. Calculated weight per shell to assess dissolution for *T. sacculifer* and *G. ruber*.

Figure S2: Pannel A) shows the various scenarios of $\delta^{11}B_{seawater}$ tested for pCO_2 reconstruction, in green Greenop et al. (2017) (G17), red Raitzsch and Hönisch, (2013) (R&H13) and in blue Lemarchand et al. (2000) (L02). Pannel B) is the reconstructed pH based our $\delta^{11}B_{carbonate}$ records associated with the different scenarios. The propagated uncertainties were calculated using eq. S14. Due to the 1‰ uncertainty propagated for $\delta^{11}B_{seawater}$, all scenarios of reconstructed seawater pH are within error of each other

Figure S3: Pannel A) shows the various scenarios of Alkalinity (e.g. second carbonate parameter) tested for pCO_2 reconstruction, in orange R-05 (Ridgwell and Zeebe, 2005), in violet T&Z-04 (Tyrell and Zeebe, 2004) and in green Caves-16 (Caves et al., 2016). Pannel B) is the reconstructed pCO2 records (based on $\delta^{11}B_{seawater}$ from scenario G17) associated with the different alkalinity scenarios, orange (Ridgwell and Zeebe, 2005), violet (T&Z-04) and green (Caves-16). The propagated uncertainties were calculated using eq. S15.

Table S1: Control points for a 2‰ offset used for *G. ruber*

	Species	Sample					mcd	mbsf	Shell Wt (µg)	Age (Ma)	SST (°C)	error (°C)	Salinity (psu)	TA (µmol/kg)	pH (total scale)	Error	pCO2 (µatm)	Error max (µatm)	Error min (µatm)
MIS 30	*G. ruber*	806	B	3	5	6	8	22.06	22.06	16.1	1.046	26.4	1.8	35.3	2241	8.16	0.09	249	72	55
	T. sacculifer	806	B	3	5	31	33	22.31	22.31	18.2	1.048	25.9	0.9	35.6	2230	8.28	0.08	164	44	35
MIS 37	*G. ruber*	806	B	4	1	71	73	26.21	26.21	17.0	1.240	26.6	1.9	35.1	2230	8.09	0.09	308	93	69
	T. sacculifer	806	B	4	1	56	58	26.06	26.06	22.2	1.233	29.8	0.9	35.6	2228	8.08	0.09	295	87	66
MIS 39	*G. ruber*	806	B	4	1	131	133	26.81	26.81	16.1	1.267	28.0	1.9	35.5	2228	8.09	0.09	308	92	69
	T. sacculifer	806	B	4	1	146	148	26.96	26.96	24.0	1.274	27.8	0.9	35.6	2219	8.07	0.09	306	93	69

311
312

Table S2: Comparaison of the control points reconstructions between *T. sacculifer* and *G.ruber* for MIS 30, 37 and 39, using different offsets (see text).

	1.8 ‰ offset			**1.85 ‰ offset**			**2.0 ‰ offset**			**2.1 ‰ offset**		
	MIS 30	**MIS 37**	**MIS 39**	**MIS 30**	**MIS 37**	**MIS 39**	**MIS 30**	**MIS 37**	**MIS 39**	**MIS 30**	**MIS 37**	**MIS 39**
ΔpCO_2 (µatm)	105	37	26	100	31	20	86	13	2	77	1	-10
ΔpH (tot scale)	-0.14	-0.02	-0.01	-0.14	-0.01	-0.003	-0.12	0.01	0.02	-0.11	0.02	0.03
ΔT (°C)	-0.02	-3.75	-0.36	0.06	-3.65	-0.27	0.31	-3.39	-0.005	0.47	-3.21	0.17

Table S3: Sensitivity tests for reconstructed pH and pCO_2 (G17, Caves-16), all results are given as the minimum and maximum variation (%) observed in our data

	Salinity	**Temperature**	**$\delta^{11}B_{carbonate}$**	**$\delta^{11}B_{seawater}$**	**Alkalinity**
pH (*G. ruber*)	0.07%	0.2-0.3%	0.2-0.5 %	0.8-1.6 %	x
pH (*T. sacculifer*)	0.07-0.08 %	0.12-0.13 %	0.1-0.5 %	0.8-1.4 %	x
pCO_2 (*G. ruber*)	0.8-1.5 %	0.02-1.5 %	5-11 %	19-25 %	5 %
pCO_2 (*T. sacculifer*)	0.8-1.4 %	0.02-0.7 %	3-12 %	19-27 %	5-7 %

257

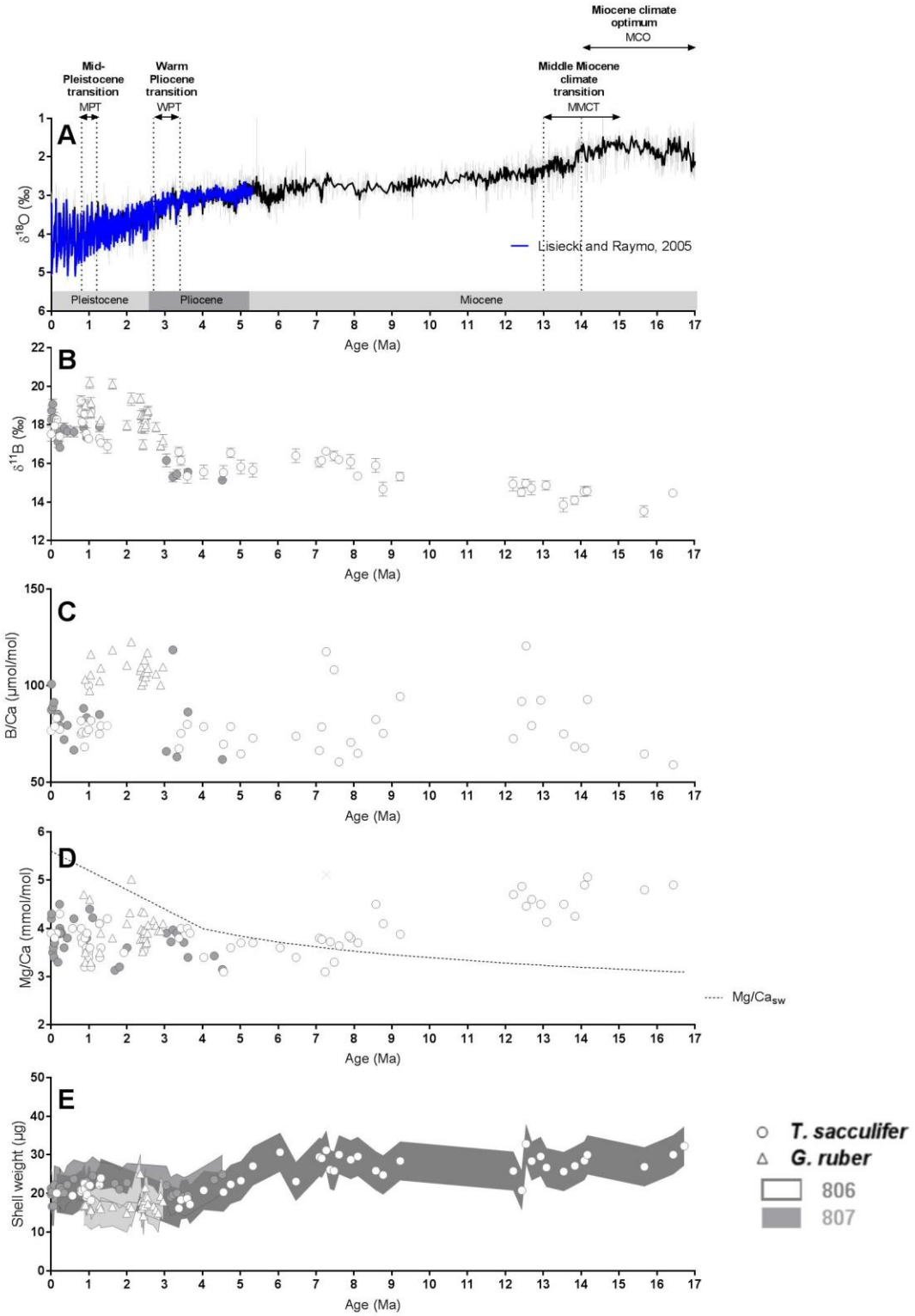

Figure S1: Results for the past 17 million years. **A.** Benthic $\delta^{18}O$ (blue line - Lisiecki and Raymo, 2005; black line – compilation from Zachos et al., 2008). **B.** $\delta^{11}B$ of *T. sacculifer* and *G. rube*r at sites 806, 807. **C.** B/Ca ratios. **D.** Mg/Ca ratios. **E.** Calculated weight per shell to assess dissolution for *T. sacculifer* and *G. ruber* from this study.

258

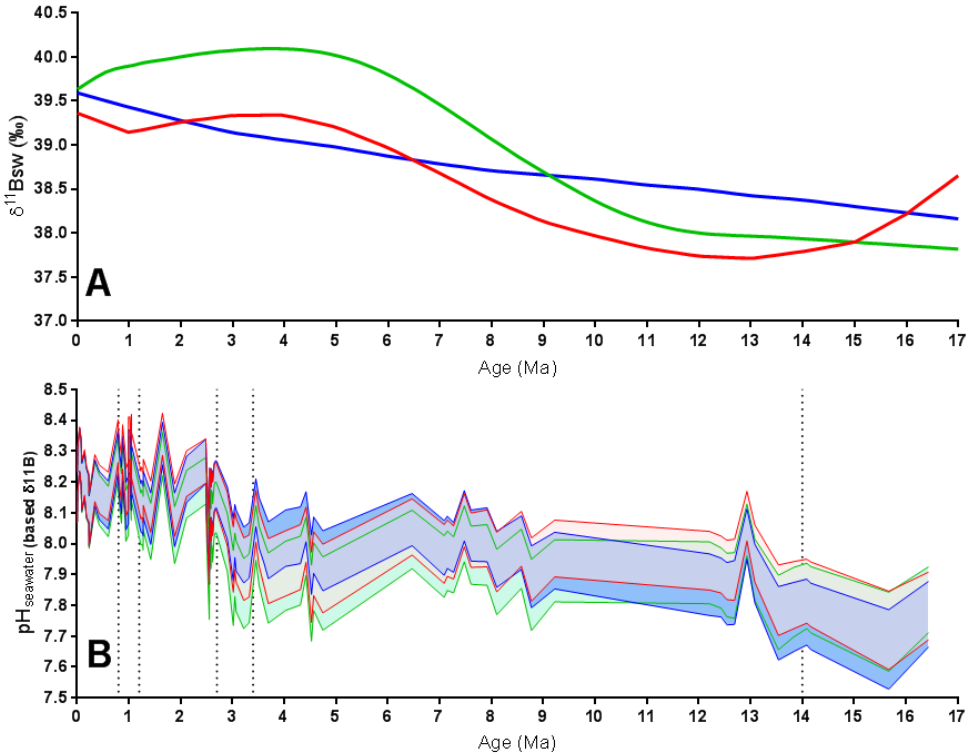

259

260

Figure S2 : Pannel A) shows the various scenarios of $\delta^{11}B_{seawater}$ tested for pCO_2 reconstruction, in green Greenop et al. (2017) (G17), red Raitzsch and Hönisch, (2013) (R&H13) and in blue Lemarchand et al. (2000) (L02). Pannel B) is the reconstructed pH based our $\delta^{11}B_{carbonate}$ records associated with the different scenarios. The propagated uncertainties were calculated using eq. S14. Due to the 1‰ uncertainty propagated for $\delta^{11}B_{seawater}$, all scenarios of reconstructed seawater pH are within error of each other.

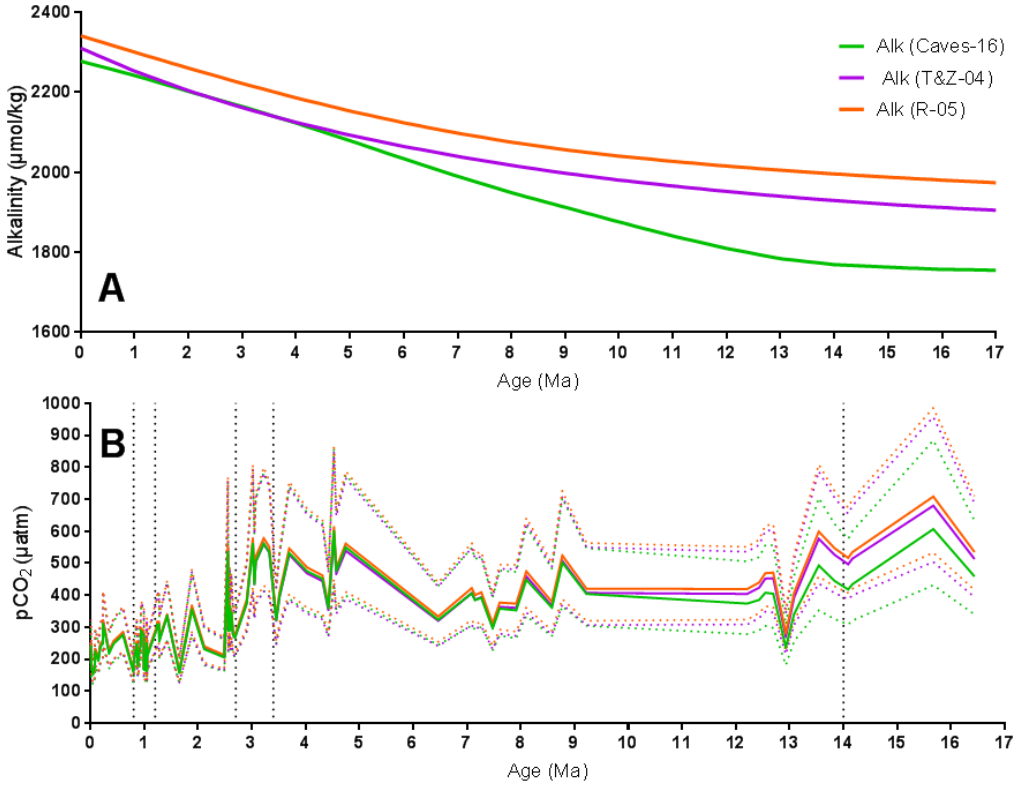

261

262 **Figure S3 :** Pannel A) shows the various scenarios of Alkalinity (e.g. second carbonate parameter) tested for pCO_2 reconstruction, in orange R-05 (Ridgwell and Zeebe, 2005), in violet T&Z-04 (Tyrell and Zeebe, 2004) and in green Caves-16 (Caves et al., 2016). Pannel B) is the reconstructed pCO2 records (based on $\delta^{11}B_{seawater}$ from scenario G17) associated with the different alkalinity scenarios, orange (Ridgwell and Zeebe, 2005), violet (T&Z-04) and green (Caves-16). The propagated uncertainties were calculated using eq. S15.